A finite-volume method for simulating contact lines on unstructured meshes in a conservative level-set framework

Savinien Pertant, Manuel Bernard, Giovanni Ghigliotti, Guillaume Balarac

Version of Record: https://www.sciencedirect.com/science/article/pii/S0021999121004770
Manuscript_c1fcba40a88f4173299102d9d2af90f9

A finite-volume method for simulating contact lines on unstructured meshes in a conservative level-set framework

Savinien Pertant[a,*], Manuel Bernard[a], Giovanni Ghigliotti[a], Guillaume Balarac[a,b]

[a] *Univ. Grenoble Alpes, CNRS, Grenoble INP, LEGI, 38000 Grenoble, France*
[b] *Institut Universitaire de France (IUF), Paris, France*

Abstract

Accurate numerical simulation of moving contact lines on complex boundaries with surface wettability effect remains a challenging problem. In this paper, we introduce a robust and accurate method to perform 3D contact line simulations on unstructured meshes with an imposed contact angle. The contact angle is imposed through a sub-grid scale curvature term and the contact line motion is enabled thanks to partial slip on the wall. Moreover, an original strategy has been designed to improve normal and curvature computation at contact line from the level-set field. The whole method is validated on 2D and 3D test cases and shows good mass conservation properties. The drop detachment from a horizontal fiber due to gravity or surface tension is then investigated. For this purpose, dynamic mesh adaptation is used to keep high resolution around the interface with moderate number of cells. These realistic cases demonstrate the ability of the numerical method to handle surface wettability effects on resolved complex geometries.

Keywords: Contact angle, Unstructured mesh, Conservative level-set, Sub-grid scale curvature, Blind spot, High-order Taylor series expansions

1. Introduction

In many two-phase flows the liquid-gas interface intersects a solid boundary, as in nucleate boiling, micro-fluidics, lubrication or two-phase flows in porous media. The contact line is defined by the intersection of the interface on the solid boundary and is characterized by a contact angle measured between the interface and the wall. The phenomena happening in this area often have a strong influence on the overall flow, such as in the case of a sliding drop on an inclined plane [51].

Numerical simulation is an interesting tool to study contact lines and contact angles because it enables to isolate a single bubble or drop, when experimental measurements can be tough. Due to the various range of scales involved (from molecular scale to drop or bubble size), several approachs may be employed to simulate contact lines. Contact lines can be simulated at the molecular scale with molecular dynamics simulations [27] or at the continuous level where the two-phase flow is governed by the Navier-Stokes equations. In this study, we investigate the second category to be able to simulate the flow at the drop scale and to account for the solid wall geometry. Over the past 20 years, various studies using different methods for the liquid-gas interface representation have been employed to simulate contact lines, such as diffuse-interface method [24], front-tracking method [22], volume-of-fluid method [46] or level-set method [52].

Even though the huge majority of the contact lines numerical studies have been performed on structured cartesian grids, some works were dedicated to simulating contact lines on unstructured meshes. The major advantage of such meshes is their ability to fit any boundary whereas the standard structured grids cannot adapt to complex geometries. Simulating contact lines on unstructured meshes enables to simulate realistic two-phase flows with accurate representation of the flow and the interface in the near wall region. The first simulations of contact angle on unstructured meshes can be found in Manservisi and Scardovelli [40] and Saha and Mitra [47]. Manservisi and Scardovelli [40] used a front-tracking method coupled with a finite element method to simulate the drop impact and spreading on a flat horizontal surface. Saha and Mitra [47] used a volume-of-fluid method coupled with finite volume method to simulate the two-phase flow in a microchannel partially filled with pillars. The diffuse-interface method has also been employed in combination with finite element method by Gao and Feng [19] to study in

*Corresponding author
Email address: savinien.pertant@univ-grenoble-alpes.fr (Savinien Pertant)

2D the propulsion of animals walking on water. Buscaglia and Ausas [5] developed a variational approach for surface tension and wetting with a level-set/finite element method which was assessed on a tetrahedral mesh. More recently, the coupled level-set and volume-of-fluid method was adapted to take contact angles into account in a finite volume framework by Dianat et al. [16]. This methodology was successfully employed to simulate a sliding drop in a curved channel discretized with a non-orthogonal mesh. To the best of the authors' knowledge, simulations of contact angles on unstructured grids with a level-set method (not coupled with volume-of-fluid method) and finite volume method does not exist in the literature so far, motivating the present study. The finite volume method furthermore naturally enforces the conservation of the fluxes between adjacent cells, ensuring conservation at the discrete level for the governing equations. Moreover, the method proposed here relies on the conservative level-set [42], improving the mass conservation properties of the standard level-set method.

Only few details on contact angle imposition and numerical particularities required for a smooth and accurate contact line evolution are available in papers using general unstructured meshes. Most studies deal with contact angle value computation through physical models, as contact angle hysteresis [32] or dynamic contact angle laws [47]. Here we emphasize the numerical method for applying a given contact angle on an unstructured mesh and for allowing the contact line slip on the wall. An original method to compute accurately the interface curvature from the level-set field in the wall neighbourhood is proposed as well. The developed method is operating on general simplicial meshes (the number of neighbouring nodes is not fixed) and enables automatic remeshing. This paper can be considered as an adaptation of the methodology for cartesian meshes recently described in Wang and Desjardins [57] to unstructured meshes. In [57], the conservative level-set is used to simulate 2D and 3D contact lines. The solid boundary, not fitting the mesh, is represented thanks to an immersed boundary method [45]. The contact angle is imposed through an appropriate curvature modification at contact line location. The methodology is validated on canonical test cases and is employed to simulate drop-fiber interaction showing good agreement with experimental results. The same test cases are investigated here to validate the new numerical method. Using a wall-conforming mesh removes the need of an immersed boundary method.

This paper is organized as follows. Section 2 introduces the governing equations of the flow, the interface conditions, the interface capturing method and the wall/contact line conditions. Section 3 details the numerical method with an emphasis on the contact line treatment. Section 4 shows the results obtained in 2D and 3D, validated against numerical and experimental results. The benefit of the unstructured mesh is demonstrated. Section 5 eventually sums up the main findings and concludes this work.

2. Governing equations

2.1. Incompressible Navier-Stokes equations

The flow is described by the incompressible Navier-Stokes equations. The mass conservation reads

$$\nabla \cdot \boldsymbol{u} = 0, \tag{1}$$

where $\boldsymbol{u}$ is the fluid velocity. Assuming uniform density in each phase, the momentum conservation reads

$$\frac{\partial \boldsymbol{u}}{\partial t} + \nabla \cdot (\boldsymbol{u} \otimes \boldsymbol{u}) = -\frac{\nabla P}{\rho} + \frac{1}{\rho}\nabla \cdot \left(\mu \left(\nabla \boldsymbol{u} + (\nabla \boldsymbol{u})^T\right)\right) + \boldsymbol{g}, \tag{2}$$

where P is the pressure, $\boldsymbol{g}$ the gravitational acceleration and ρ and μ respectively the density and the dynamic viscosity of the considered phase. The material properties are considered constant and uniform in each phase.

2.2. Liquid-gas interface conditions

The discontinuity of a per-phase uniform field A at liquid-gas interface Γ is defined as $[A]_\Gamma = A_{liq} - A_{gas}$. Without phase change, the velocity is continuous across the interface, i.e. $[\boldsymbol{u}]_\Gamma = \boldsymbol{0}$. The interfacial pressure jump is given by [56]

$$[P]_\Gamma = \sigma\mathcal{K} + [\mu]_\Gamma \ (\boldsymbol{n}_\Gamma)^T \left(\nabla \boldsymbol{u} + (\nabla \boldsymbol{u})^T\right) \boldsymbol{n}_\Gamma \tag{3a}$$

$$= \sigma\mathcal{K} + 2\,[\mu]_\Gamma \frac{\partial u_n}{\partial n}, \tag{3b}$$

where σ is the uniform surface tension coefficient between liquid and gas (Marangoni effect is neglected), $\boldsymbol{n}_\Gamma$ the interface normal vector and $\mathcal{K}$ the local interface curvature. $\frac{\partial u_n}{\partial n}$ is the derivative of the velocity

normal component in the interface normal direction. The interface curvature can be defined as the sum of the two principal curvatures and is computed as

$$\mathcal{K} = -\nabla \cdot \boldsymbol{n}_\Gamma. \tag{4}$$

For any unit tangent vector to the interface $\boldsymbol{t}_\Gamma$, the tangential stress condition is also given by [56]

$$-\left[\mu\right]_\Gamma \left(\boldsymbol{t}_\Gamma\right)^T \left(\nabla \boldsymbol{u} + \left(\nabla \boldsymbol{u}\right)^T\right) \boldsymbol{n}_\Gamma = \left(\boldsymbol{t}_\Gamma\right)^T \nabla_s \sigma = 0, \tag{5}$$

where the surface gradient $\nabla_s \sigma$ is always null since Marangoni effect is neglected. The tangential stress is thus continuous across the interface.

2.3. Liquid-gas interface capturing method: conservative level-set

The liquid-gas interface is captured by a level-set method [44]. In the standard level-set method, the interface is implicitely represented as the 0 isocontour of the signed distance function to the interface. In this study, we use the more recent conservative level-set method [42, 43, 15]. The interface is represented as the $\psi = 0.5$ isocontour of the function

$$\psi(\boldsymbol{x}, t) = \frac{1}{2}\left(\tanh\left(\frac{\phi(\boldsymbol{x}, t)}{2\varepsilon}\right) + 1\right), \tag{6}$$

where $\phi(\boldsymbol{x}, t)$ is the signed distance function to the interface (positive-definite in the liquid) and 2ε is the thickness of this smoothed Heaviside profile, defined as the cell size. This sharp profile is advected in a conservative manner by solving

$$\frac{\partial \psi}{\partial t} + \nabla \cdot (\boldsymbol{u}\psi) = 0, \tag{7}$$

where the assumption $\nabla \cdot \boldsymbol{u} = 0$ has been used to transform the advection equation in a conservative equation. One of the major issues with this approach is that after advection, the profile is not a hyperbolic tangent anymore due to non uniformity of the flow and numerical errors [42]. In order to reshape the profile without moving the interface position, a conservative re-initialization equation was developed by Olsson and Kreiss [42] and successively improved by [43, 15, 7]. In this work, the re-initialization equation reads [7]

$$\frac{\partial \psi(\tau, \boldsymbol{x})}{\partial \tau} = \nabla \cdot \left(\frac{1}{4\cosh^2\left(\frac{\phi_{\text{map}}(\tau, \boldsymbol{x})}{2\varepsilon}\right)} \left(\nabla \phi_{\text{map}}(\tau, \boldsymbol{x}) \cdot \boldsymbol{n}_\Gamma(t, \boldsymbol{x}) - 1\right) \boldsymbol{n}_\Gamma(t, \boldsymbol{x})\right), \tag{8}$$

and is solved in pseudo-time τ until steady state. ϕ_{map} is a signed distance function mapped from the conservative level-set with

$$\phi_{\text{map}}(\tau, \boldsymbol{x}) = \varepsilon \ln\left(\frac{\psi(\tau, \boldsymbol{x})}{1 - \psi(\tau, \boldsymbol{x})}\right), \tag{9}$$

which is the inverse function of Eq. (6). The interface normal vector, kept constant during the re-initialization process, is defined as

$$\boldsymbol{n}_\Gamma(t, \boldsymbol{x}) = \frac{\nabla \phi(t, \boldsymbol{x})}{||\nabla \phi(t, \boldsymbol{x})||}, \tag{10}$$

where $||\nabla \phi(t, \boldsymbol{x})|| = 1$ for an exact distance field. The right-hand side of re-initialization Eq. (8) vanishes when $\nabla \phi_{\text{map}}(\tau, \boldsymbol{x}) = \boldsymbol{n}_\Gamma(t, \boldsymbol{x})$. This equation tends then to align the ϕ_{map} function with the signed distance function ϕ. The re-initialized ψ function is thus the hyperbolic tangent profile built on the signed distance function. The transport and re-initialization equations being written in a conservative manner, this highly improves mass conservation which is the main drawback of the standard signed distance level-set method [42]. However this method requires to compute additionally the signed distance function to evaluate the normal vector with Eq. (10), which can be an issue close to the contact lines as detailed in section 3.

2.4. Fluid-solid interface

On a solid boundary, the non-penetration condition $\boldsymbol{u}_\perp = (\boldsymbol{u} \cdot \boldsymbol{n}_{wall})\, \boldsymbol{n}_{wall} = \boldsymbol{0}$ is applied, where $\boldsymbol{n}_{wall}$ is the wall normal unit vector. It is well-known that the use of the classic no-slip condition on the wall does not allow the contact line to move, due to the null advection velocity $\boldsymbol{u}_{||} = \boldsymbol{u} - \boldsymbol{u}_\perp$ on the wall.

It was furthermore theoretically shown that it leads to an infinite viscous force at contact line [23]. One must note that on the particular case of cartesian staggered grids, the cell face velocity stored at $\Delta/2$ above the wall is used to transport the contact line (either in VOF or level-set), alleviating the problem

because this cell face velocity is never imposed to 0 but is such that the extrapolated velocity on the wall would be 0, as explained by Afkhami et al. [1]. Nevertheless, this does not lead to mesh convergent results regarding contact line dynamics. Furthermore, in the context of collocated node-centered meshes where the velocity used to transport the contact line is stored at nodes on the wall, the problem remains unsolved. A common way to solve this issue is to replace the no-slip condition by a partial slip condition, defined as

$$\boldsymbol{u}_{||} = \lambda \left. \frac{\partial \boldsymbol{u}_{||}}{\partial y} \right|_{wall}, \tag{11}$$

where y is the wall normal coordinate and λ a slip length. This Robin boundary condition, known as Navier slip condition, enables the contact line to slip on the wall. The implementation of this condition and the choice of the slip length are detailed in section 3.2.

2.5. Contact angle

For a static or uniformly moving contact line, the contact angle value arises from the equilibrium between the interfacial forces in the plane of the wall, given by the Young-Dupré law [60]

$$\gamma_{SG} - \gamma_{SL} - \sigma \cos\left(\theta_{eq}\right) = 0, \tag{12}$$

where γ_{SG} and γ_{SL} are respectively the surface tension coefficients between solid and gas and between solid and liquid. The equilibrium contact angle θ_{eq} is measured in the liquid. This law is only valid for an ideal surface, flat, perfectly smooth and chemically homogeneous. On a real surface, the contact angle is not unique, leading for instance to hysteresis phenomenon, i.e. a different angle between advancing and receding contact line [11]. In this study, the contact angle is considered uniform and constant, being imposed as an external parameter to take into account the wettability of the solid surface.

3. Numerical method

The code YALES2, a library of finite-volume node-centered low Mach number solvers, has been used for this work [41]. This massively parallel code is able to simulate turbulent and reactive two-phase flows in industrial configurations on unstructured grids with several billions elements. The numerical method to solve the unsteady incompressible Navier-Stokes equations is based on the projection method initially proposed by Chorin [8, 9] and Temam [55] for pressure-velocity coupling. The time integration of the transport equations is performed with the TFV4A scheme developed by Kraushaar [28]. More specifically, the two-phase flow solver based on conservative level-set method [42] and ghost-fluid method [18] has been used and modified for simulating contact lines in this study.

3.1. Contact angle implementation

To account for surface wettability effect, an additional constraint must be added at contact line location to force the interface to respect the imposed contact angle. With the aim of developing a method to impose a prescribed contact angle, we consider in this work a uniform and constant contact angle. Furthermore, we do not make the distinction between the macroscopic contact angle, measured at droplet scale, and microscopic contact angle, measured at molecular scale where interfacial forces balance. However, the employed method can be generalised to more complicated models. A common method, first introduced by Brackbill et al. [4] in a volume-of-fluid framework and used more recently by Legendre and Maglio [30], is known as wall adhesion boundary method. It consists in imposing a boundary condition on $\boldsymbol{n}_\Gamma$ at the wall where this normal vector corresponds to the imposed contact angle and not to the contact angle measured through the level-set function. The curvature computed with Eq. (4) is thus modified by the boundary condition and a capillary force appears as a result. The contact angle is imposed implicitely, through the modification of the curvature. A similar method was proposed in the context of level-set method by [12, 13, 37] and recently applied by Wang and Desjardins [57] on 3D cartesian meshes to simulate contact lines on complex geometries using conservative level-set and an immersed boundary method to represent the fluid-solid interface. The curvature at contact line is corrected by a sub-grid scale curvature designed for contact angle imposition, i.e.

$$\mathcal{K}_{CL} = \mathcal{K}_{RES} + \mathcal{K}_{SGS}, \tag{13}$$

where $\mathcal{K}_{RES}$ is the resolved curvature defined by Eq. (4). Through the pressure jump Eq. (3), this correction modifies the pressure gradient and as a consequence the flow in the contact line vicinity. The sub-grid scale curvature, here adapted to an unstructured grid, is defined as

$$\mathcal{K}_{SGS} = -\frac{\boldsymbol{n}_{\Gamma,CL} \cdot \boldsymbol{n}_{wall,CL} + \cos\left(\theta_{eq}\right)}{h}, \tag{14}$$

where $\boldsymbol{n}_{\Gamma,CL}$ is the interface normal at contact line, $\boldsymbol{n}_{wall,CL}$ is the inward wall normal vector at contact line, θ_{eq} the imposed contact angle in the liquid and h is half of the cell size averaged in a narrow band around contact line, to be consistent with the definition of $\mathcal{K}_{SGS}$ given in [57]. Since $\boldsymbol{n}_{\Gamma,CL} \cdot \boldsymbol{n}_{wall,CL} = -\cos(\theta_{measured})$, the curvature is proportionnal to the imbalance between measured contact angle and imposed contact angle, resulting in a bending of the interface close to the wall to respect the desired angle. The evaluation of the interface normal vector close to the contact line needs specific treatment which will be discussed below. The accuracy of the sub-grid scale curvature evaluation is of major importance to impose the contact angle properly. It is evaluated at the same position as the resolved curvature to be consistent with Eq. (13), i.e. directly at contact line. The main advantage of this method, as the wall adhesion method, is that it directly acts on the capillary force to impose the contact angle without modifying the level-set field, preventing possible mass conservation issues and spurious displacements of the contact line.

3.2. Navier slip boundary condition

The Navier slip condition is used to allow the contact line motion on the solid wall. We recall the expression of the boundary condition for the slip velocity

$$\boldsymbol{u}_{||} = \lambda \left. \frac{\partial \boldsymbol{u}_{||}}{\partial y} \right|_{wall}. \tag{15}$$

A realistic order of magnitude for the slip length is $\lambda \sim 1$ nm since slip occurs at molecular scale [29]. If the slip length is not resolved by the mesh resolution, results are mesh-dependent as shown by Spelt [52] and Afkhami et al. [1]. An accurate simulation of the contact line dynamics in a simulation at the scale of a drop would therefore need a tremendous number of cells. Several studies have focused on mesh-independent contact line dynamics with reasonable number of cells, using for instance contact angle mesh-dependent models [1, 17, 53, 30, 51]. This physical modelling is beyond the scope of our study, even if the numerical framework presented hereafer could be enriched with such a modelling in the future. Unless specified, for a given case we set $\lambda = \overline{\Delta}_{coarse}$, with $\overline{\Delta}_{coarse}$ the cell size average on the wall for the coarsest mesh simulated for this given case. This ensures that the slip length is always resolved, preventing mesh dependency, despite being overestimated.

On unstructured grids, the velocity gradient in Eq. (15) has to be carefully defined. Some useful notations are defined on Fig. 1. The wall-velocity gradient is computed per element $\mathrm{El_i}$ in contact with

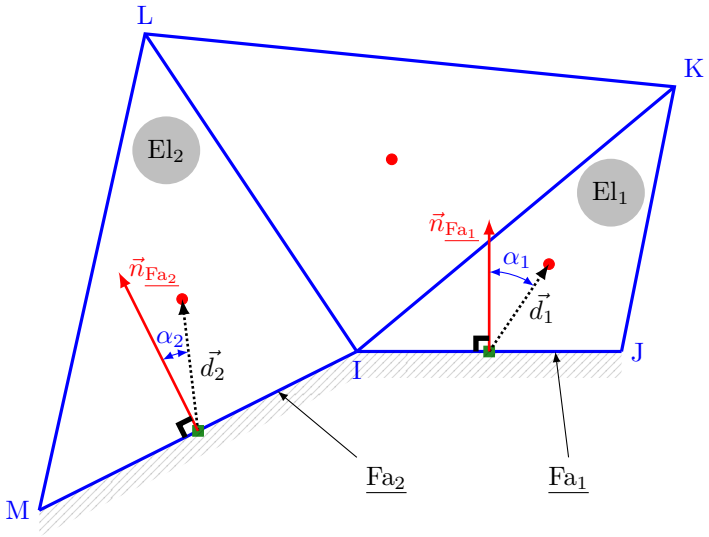

Figure 1: Definition of the notations for the wall-velocity gradient computation in 2D.

the wall, with

$$\left. \frac{\partial \boldsymbol{u}}{\partial y} \right|_{wall}^{\mathrm{El_i}} = \frac{\boldsymbol{u}_{\mathrm{El_i}} - \boldsymbol{u}_{\underline{\mathrm{Fa_i}}}}{||\boldsymbol{d}_i||} \cos(\alpha_i), \tag{16}$$

where $\boldsymbol{u}_{\mathrm{El_i}}$ is the average element velocity based on nodal velocities, $\boldsymbol{u}_{\underline{\mathrm{Fa_i}}}$ the velocity at the wall face $\underline{\mathrm{Fa_i}}$, $\boldsymbol{d}_i$ the vector between the wall face center and the element barycenter and α_i the angle between the wall face normal vector $\boldsymbol{n}_{\underline{\mathrm{Fa_i}}}$ and $\boldsymbol{d}_i$. The norm of $\boldsymbol{n}_{\underline{\mathrm{Fa_i}}}$ is half of the wall face surface, i.e. $||\boldsymbol{n}_{\underline{\mathrm{Fa_1}}}|| = ||\boldsymbol{IJ}||/2$.

This gradient computed along $\boldsymbol{d}_i$ is projected in the wall normal direction, taking the element deformation into account. On a wall face, one should discretize Eq. (15) at iteration $n+1$ with

$$\boldsymbol{u}_{\underline{\mathrm{Fa_i}}}^{n+1} = \lambda \frac{\boldsymbol{u}_{\mathrm{El_i}}^{n+1} - \boldsymbol{u}_{\underline{\mathrm{Fa_i}}}^{n+1}}{||\boldsymbol{d}_i||} \cos(\alpha_i), \tag{17}$$

Such an implicit implementation would require an iterative method to find $\boldsymbol{u}_{\underline{\mathrm{Fa_i}}}^{n+1}$. On the other hand, we found that if the right-hand side of Eq. (17) is written at iteration n the simulations are unstable. An intermediate and easy formulation consists in making the assumption $\boldsymbol{u}_{\mathrm{El_i}}^{n+1} \simeq \boldsymbol{u}_{\mathrm{El_i}}^{n}$. This allows to write the explicit boundary condition

$$\boldsymbol{u}_{\underline{\mathrm{Fa_i}}}^{n+1} = \frac{\lambda}{\frac{||\boldsymbol{d}_i||}{\cos(\alpha_i)} + \lambda} \boldsymbol{u}_{\mathrm{El_i}}^{n}. \tag{18}$$

This formulation introduces a first order error with respect to Δt, however, as seen in section 4.3 the error due to time discretization is not dominant. A similar discretization of the slip velocity is employed in [1]. Since $\boldsymbol{u}_{\underline{\mathrm{Fa_i}}}^{n+1}$ may not be parallel to the wall, the wall-normal component is then removed

$$\boldsymbol{u}_{\underline{\mathrm{Fa_i}},||}^{n+1} = \boldsymbol{u}_{\underline{\mathrm{Fa_i}}}^{n+1} - \left(\boldsymbol{u}_{\underline{\mathrm{Fa_i}}}^{n+1} \cdot \frac{\boldsymbol{n}_{\underline{\mathrm{Fa_i}}}}{||\boldsymbol{n}_{\underline{\mathrm{Fa_i}}}||} \right) \frac{\boldsymbol{n}_{\underline{\mathrm{Fa_i}}}}{||\boldsymbol{n}_{\underline{\mathrm{Fa_i}}}||}. \tag{19}$$

Finally, the nodal velocity at wall is computed as the average of the wall face velocities weighted by $||\boldsymbol{n}_{\underline{\mathrm{Fa_i}}}||$

$$\boldsymbol{u}_{I,||}^{n+1} = \frac{||\boldsymbol{n}_{\underline{\mathrm{Fa_1}}}||\, \boldsymbol{u}_{\underline{\mathrm{Fa_1}},||}^{n+1} + ||\boldsymbol{n}_{\underline{\mathrm{Fa_2}}}||\, \boldsymbol{u}_{\underline{\mathrm{Fa_2}},||}^{n+1}}{||\boldsymbol{n}_{\underline{\mathrm{Fa_1}}}|| + ||\boldsymbol{n}_{\underline{\mathrm{Fa_2}}}||}. \tag{20}$$

The extension to 3D is straightforward. Note that in 3D the wall nodes can be connected to an arbitrary number of wall faces. The implementation of the Navier slip boundary condition is validated on a laminar channel single-phase flow detailed in AppendixA. Convergence with mesh refinement is found.

3.3. Curvature and normal computation

Whatever the level-set method used to capture the interface, one needs to calculate the distance to the interface to compute the normal and curvature. Using the definition of the normal vector Eq. (10) and expanding Eq. (4), we obtain the formula given by Goldman [20] for the curvature

$$\mathcal{K} = \frac{\nabla\phi^{\mathrm{T}}\, \nabla\nabla\phi\, \nabla\phi - ||\nabla\phi||^2\, \mathrm{Tr}\left(\nabla\nabla\phi\right)}{||\nabla\phi||^3}, \tag{21}$$

where $\mathrm{Tr}(\cdot)$ is the trace of a matrix and $\nabla\nabla\phi$ the hessian of distance. The accuracy of distance computation and differential operators applied to distance is of major importance for curvature estimate. In this study, the signed distance function is computed with a second-order geometrical method developed in Janodet et al. [25] for unstructured simplicial meshes. By means of an orthogonal projection of the nodes on the interface and propagation of the information away form the interface using the principle of fast marching method, ϕ is built as the exact distance to the discretized interface which is a set of segments (2D) or triangles (3D).

3.3.1. Blind Spot identification

When dealing with contact lines, however, there is a zone named *Blind Spot* where the orthogonal distance to the interface is not defined on the obtuse side of the contact angle [14], as shown in Fig. 2. This region is defined by the set of points that do not have an orthogonal projection on the interface due to the presence of the boundary. One can define the distance in the Blind Spot as the distance to the closest piece of interface. This is naturaly done in the context of geometric distance algorithm, where the distance in the Blind Spot is given as the distance to the contact line, which is the closest piece of interface for all the nodes in the Blind Spot. As a result, the isocontours of distance form circles centered around the contact line (in 2D) in the Blind Spot and are highly curved (see Fig. 2), resulting in a spurious curvature evaluation at contact line and as a consequence poor contact line dynamics. A similar problem appears when the distance is computed with a Hamilton-Jacobi equation: the problem is not well-posed because it lacks boundary conditions [14]. Thus, whatever the method used to compute the distance (Geometric, Fast Marching Method or Hamilton-Jacobi), one needs to correct ϕ in the Blind Spot for accurate normal and curvature computation around the contact line.

It should be noted that there is no *correct* distance evaluation in the Blind Spot, since distance is not correctly defined there. The only objective to define the distance field in the Blind Spot is to be able to

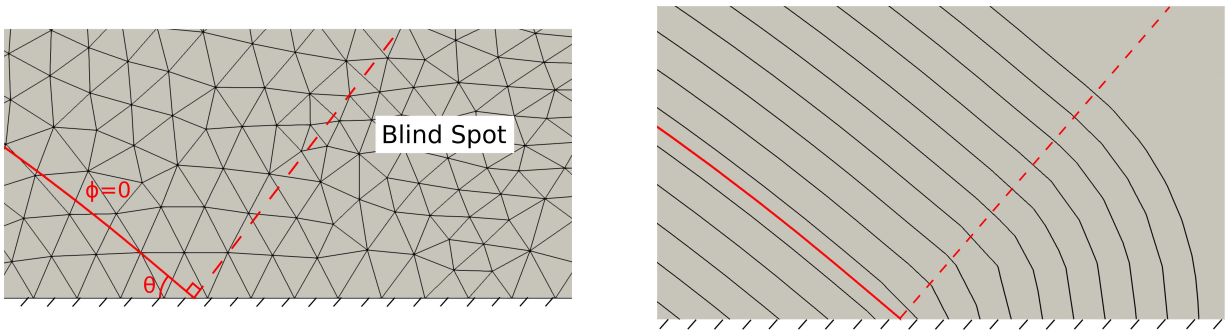

Figure 2: Left: Definition of the Blind Spot. The red solid line is the interface and the red dashed line delimits the Blind Spot. Here the Blind Spot is delimited by the line normal to the interface passing through the contact line but it is not always the case for interfaces having a non uniform curvature close to the wall. Right: Isocontours of distance in the Blind Spot (black solid lines).

correctly compute the normal and the curvature of the interface close to the contact line. It appears that a first method to correct the distance in the Blind Spot would be to build a linear ghost interface inside the wall based on the contact angle and the contact line position, and then compute the distance to this extended interface in the Blind Spot [52]. Nevertheless, this method is difficult to extend to 3D since it would require the construction of complex surfaces. Furthermore, while improving the normal vector computation in the Blind Spot, the distance built on a linear extrapolation of the interface is not enough for accurate curvature evaluation. Using a distance computed through the resolution of a Hamilton-Jacobi equation, Della Rocca and Blanquart [14] proposed to apply an appropriate boundary condition on the wall for the re-distance equation which enables to populate the Blind Spot with a correct distance. The information is thus propagated from the wall to the Blind Spot. This algorithm was successfully tested on cartesian meshes. However, such a method cannot be applied to our distance computation based on geometric operations and for which no propagation equation is solved. Owing to this particularity, the strategy proposed in this study is first to identify all nodes of the Blind Spot to correct their distance at a later stage.

To this purpose, we slightly modify the distance computation algorithm of Janodet et al. [25] to add the information if a node belongs to the Blind Spot or not. For each node, we check if the computed distance corresponds to the distance to a piece of interface intersecting the wall. In this case, we check if the distance to the interface is equal to the distance to the intersection between the piece of interface and the wall, which is the contact point (2D) or a piece of the contact line (3D). As a result, all the nodes for which the distance to the interface is equal to the distance to the contact line are considered in the Blind Spot. An example in 2D is given in Fig. 3a. The projection of node 1 is on a segment of interface which does not intersect the wall, so it does not belong to the Blind Spot. The projection of node 2 is on a segment intersecting the wall but the projection is not on the wall, so it does not belong to the Blind Spot. For node 3, the orthogonal projection on the interface is not defined and the closest piece of interface to this node is the contact point. The distance to the interface is thus equal to the distance to the contact point, therefore it belongs to the Blind Spot. This method works in 2 and 3 dimensions whatever the complexity of the interface shape. A 2D example of the Blind Spot field after identification is given in Fig. 3b.

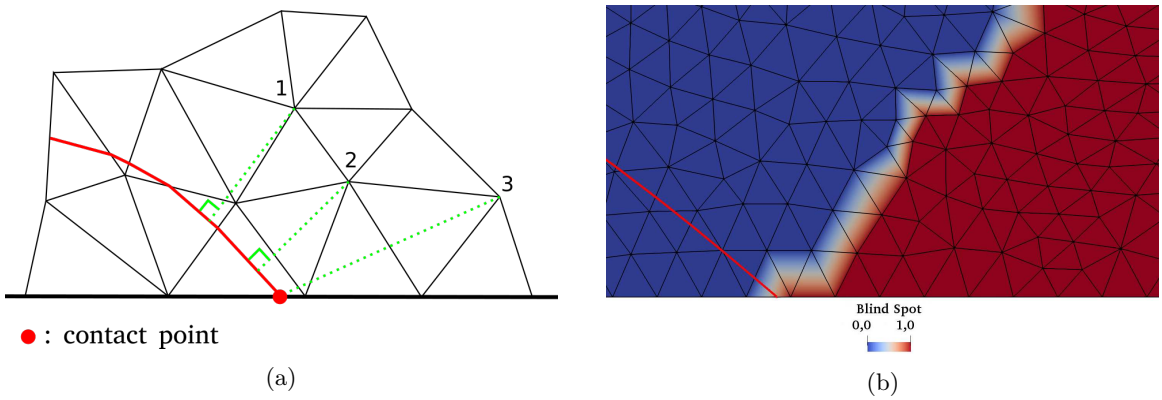

(a) (b)

Figure 3: Identification of the Blind Spot nodes. (a) Identification procedure. Node 3 belongs to the Blind Spot whereas nodes 1 and 2 do not. (b) Blind Spot field after identification (1 in the Blind Spot, 0: not in the Blind Spot).

3.3.2. Distance extension

The identification of the nodes belonging to the Blind Spot allows to manipulate the distance function in order to accurately compute the interface normal vector and curvature. As stated before, without correction, the distance field equal to the distance to the contact line in the Blind Spot leads to a bad normal vector and curvature evaluation close to the contact lines, resulting in incorrect contact angle estimation and contact line dynamics. A natural way to populate the Blind Spot nodes with a suitable distance field is to extend the distance from nodes where it is correctly computed (i.e. outside the Blind Spot) to the Blind Spot. To this purpose, we perform multi-dimensional Taylor series expansions to populate the Blind Spot with an extrapolated distance. The accuracy of these expansions being highly dependent on the evaluation of the nodal differential operators, we use high-order finite volume differential operators developed by Bernard et al. [2] to compute the gradient and the hessian of distance. This method enables to compute second-order gradient and first-order hessian on unstructured simplicial meshes from an analytical field. Furthermore, those differential operators are computed with a compact stencil: a node only needs information from its direct neighbours. It leads to high parallel performance. The procedure to compute the distance in the Blind Spot is detailed hereinafter. First, we consider a pseudo-interface separating the Blind Spot from the rest of the domain. A band is then defined, ordering nodes on both sides of the pseudo-interface, based on their connectivity, as illustrated on Fig. 4. The

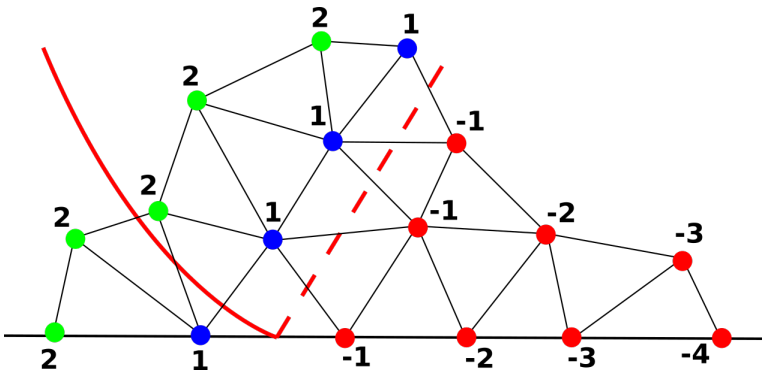

Figure 4: Nodes ordering in the Blind Spot for Taylor series expansions. The band is written next to the nodes. The red nodes are in the Blind Spot, the blue nodes are the Blind Spot neighbours and the green nodes are the Blind Spot neighbours of neighbours.

interface lies between band 1, located where distance is correctly computed, and band -1 nodes, first row of nodes in the Blind Spot. The extrapolation procedure is summed-up here :

1. Hessian and gradient of distance are extended from band 2 to band 1 nodes respectively with $\nabla\nabla\phi_1 = \nabla\nabla\phi_2 + \mathcal{O}(\Delta_{2,1})$ and $\nabla\phi_1 = \nabla\phi_2 + \nabla\nabla\phi_2\,\boldsymbol{\Delta}_{2,1} + \mathcal{O}\left(\Delta_{2,1}^2\right)$, where $\boldsymbol{\Delta}_{2,1} = \boldsymbol{x}_1 - \boldsymbol{x}_2$ is the vector between node of band 2 and node of band 1. If the node of band 1 is connected to several nodes of band 2, their contributions are averaged.

2. Hessian, gradient and distance are extended from band 1 to band -1 nodes. The order 3 Taylor series expansion of distance reads

$$\phi_{-1} = \phi_1 + \boldsymbol{\Delta}_{1,-1}\cdot\nabla\phi_1 + \frac{1}{2}\left(\boldsymbol{\Delta}_{1,-1}\otimes\boldsymbol{\Delta}_{1,-1}\right) : \nabla\nabla\phi_1 + \mathcal{O}\left(\Delta_{1,-1}^3\right), \tag{22}$$

   where $\otimes$ is the outer product and : the double-dot product.

3. Hessian, gradient and distance are extended from band i to band $i-1$ nodes, starting from $i=-1$ and looping until all the nodes in the Blind Spot are covered.

Remark 1. *Step 1 is necessary because the computation of differential operators at node of band 1 requests distance at node of band -1, which is initially incorrect.*

Remark 2. *In step 3, it can happen that a band $i-1$ node is not connected to any band i node. In this case, the Taylor series expansion is performed from already corrected $i-1$ nodes to the singular $i-1$ node.*

We underline the fact that this methodology does not require any ghost cells inside the wall to populate the Blind Spot. Expansions are performed in a narrow band around the interface because the resulting fields are only used at interface, for curvature and sub-grid scale curvature evaluation. As illustrated on Fig. 5, we obtain an accurate and smooth distance field in the neighbourhood of the interface.

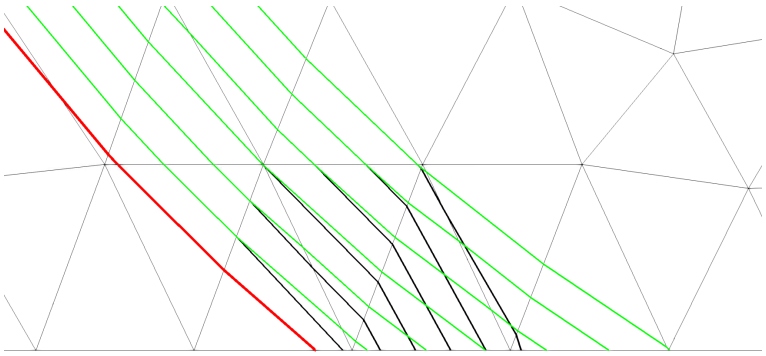

Figure 5: Distance extensions in the Blind Spot. The red solid line is the interface, the black solid lines are the isocontours of distance prior to extension (i.e. due to the geometric distance algorithm) and the green solid lines are the isocontours of distance after extension.

3.3.3. Interpolation at interface

The pressure jump $[P]_\Gamma$ being defined at the interface position, the curvature also has to be evaluated at the interface position. In general, the curvature is evaluated at nodes and it corresponds to the curvature of the isocontour of distance passing through the node. It is then interpolated at the interface position on the edge connecting two nodes. The interpolation, weighted by the distance to the interface, can be linear with the curvature or with the radius of curvature [7]. Here we use another method, based on high-order differential operators and Taylor series expansions [2]. If an edge connecting the nodes i and $i+1$ is crossed by the interface, we first extrapolate $\nabla\phi$ and $\nabla\nabla\phi$ from both nodes to the interface position

$$\begin{cases} \nabla\phi_{\Gamma,i} = \nabla\phi_i + \nabla\nabla\phi_i \, \boldsymbol{\Delta}_{i,\Gamma} + \mathcal{O}\left(\Delta_{i,\Gamma}^2\right), & \text{(23a)} \\ \nabla\phi_{\Gamma,i+1} = \nabla\phi_{i+1} + \nabla\nabla\phi_{i+1} \, \boldsymbol{\Delta}_{i+1,\Gamma} + \mathcal{O}\left(\Delta_{i+1,\Gamma}^2\right), & \text{(23b)} \end{cases}$$

and

$$\begin{cases} \nabla\nabla\phi_{\Gamma,i} = \nabla\nabla\phi_i + \mathcal{O}\left(\Delta_{i,\Gamma}\right), & \text{(24a)} \\ \nabla\nabla\phi_{\Gamma,i+1} = \nabla\nabla\phi_{i+1} + \mathcal{O}\left(\Delta_{i+1,\Gamma}\right). & \text{(24b)} \end{cases}$$

Extrapolations from both nodes are then averaged as

$$\begin{cases} \nabla\phi_\Gamma = \theta\,\nabla\phi_{\Gamma,i+1} + (1-\theta)\,\nabla\phi_{\Gamma,i}, & \text{(25a)} \\ \nabla\nabla\phi_\Gamma = \theta\,\nabla\nabla\phi_{\Gamma,i+1} + (1-\theta)\,\nabla\nabla\phi_{\Gamma,i}, & \text{(25b)} \end{cases}$$

where

$$\theta = \frac{x_\Gamma - x_i}{x_{i+1} - x_i} \tag{26}$$

is the interface relative position on the edge connecting the two nodes. Finally, the curvature is computed directly at interface with Eq. (21) applied at $\boldsymbol{x} = \boldsymbol{x}_\Gamma$.

To assess the accuracy of the curvature computation at contact line, a simple 2D test is designed. A circular interface is initialized, forming an angle θ_{eq} with a flat surface, measured inside the circle. The curvature at contact line is not corrected with the sub-grid scale curvature defined in section 3.1. The L^∞ norm of relative error on the curvature evaluated at one contact line is computed. Three configurations are tested :

A. The distance is computed with the second-order geometrical method of [25] without extensions in the Blind Spot.

B. The distance is computed with the second-order geometrical method of [25] with extensions in the Blind Spot described in section 3.3.2.

C. The distance is set to its analytical value outside the Blind Spot and is extended in the Blind Spot, using the analytical distance outside the Blind Spot.

The test is performed for the angles $\theta_{eq} = 20°$ with radius $R_0 = 0.1$ m and $\theta_{eq} = 160°$ with radius $R_0 = 0.01$ m on five meshes identified by the average cell size $\overline{\Delta}$. The radii are different to ensure that the volume of liquid is of the same order between both angles, making thus possible the use of a domain of same size. Extreme contact angle values are chosen to underline the effect of the extensions. The errors are gathered in Table 1 and 2. It can be seen that the curvature error diverges with mesh

$\overline{\Delta}$ (m)	4×10^{-3}	2×10^{-3}	1×10^{-3}	5×10^{-4}	2.5×10^{-4}
A	791.24%	2319.32%	3809.32%	5505.42%	10665.98%
B	1.73%	12.29%	0.64%	5.20%	1.80%
C	3.99%	1.81%	0.93%	0.44%	0.26%

Table 1: L^∞ error on curvature at contact line for a contact angle $\theta_{eq} = 20°$ in 2D.

$\overline{\Delta}$ (m)	4×10^{-3}	2×10^{-3}	1×10^{-3}	5×10^{-4}	2.5×10^{-4}
A	13.18%	189.19%	558.30%	571.53%	1124.28%
B	34.86%	12.87%	2.04%	3.22%	3.54%
C	38.10%	14.35%	5.42%	3.20%	0.95%

Table 2: L^∞ error on curvature at contact line for a contact angle $\theta_{eq} = 160°$ in 2D.

refinement without the Blind Spot extensions (case A). The extensions enable to decrease by several orders of magnitude the error on fine meshes, but no clear convergence is observed (case B). This can be explained by the second-order distance which leads to a constant error in curvature with mesh refinement due to the two successive differentiations. Indeed, when the distance is exact outside the Blind Spot, the curvature at contact line converges at order 1 (case C). This shows that the developed methodology, including the Blind Spot identification and distance extensions is convergent. Also, one must note that obtaining a third-order distance, and more generally a convergent curvature estimate on unstructured grids remains a challenging problem and is beyond the scope of this paper [6, 59]. The results obtained for similar cases in 3D are given in AppendixB, with the same conclusions as in 2D.

3.4. Conservative level-set

The conservative levet-set algorithm with re-initialization Eq. (8) was adapted to unstructured meshes in a finite volume framework by Janodet et al. [25]. This version is now implemented in the main YALES2 two-phase flow solver. Following [25], the re-initialization Eq. (8) is discretized as

$$\frac{\psi_i^{n^*+1} - \psi_i^{n^*}}{\Delta\tau} = \frac{1}{V_i} \sum_{ik \ edges \ of \ i} \left(\frac{1}{4\cosh^2\left(\frac{\phi_{\mathrm{map},ik}}{2\varepsilon_{ik}}\right)} \left(\nabla\phi_{\mathrm{map},ik} \cdot \boldsymbol{n}_{\Gamma,ik} - 1\right) \right) \boldsymbol{n}_{\Gamma,ik} \cdot \mathbf{d}\boldsymbol{A}_{ik}, \tag{27}$$

where n^* is the pseudo-iteration index and where the integration over the control volume V_i and the divergence theorem have been applied. It has been found that 3 pseudo-iterations are enough to reach steady state [25]. The control volume and the surface vector $\mathbf{d}\boldsymbol{A}_{ik}$ definition are illustrated on Fig. 6. It

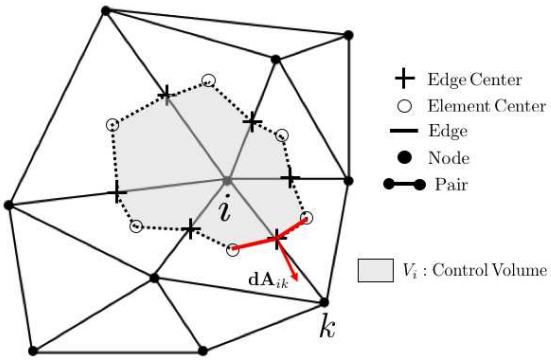

Figure 6: Control volume used for spatial integration of re-initialization equation. Reprinted from [25].

is of major importance that the right-hand side of Eq. (27) is solved with high accuracy to prevent the interface to be deformed during re-initialization. It is especially the case at contact line position where one needs to impose a contact angle and where the re-initialization process should not affect the contact line dynamics. As detailed in the following section, the re-initialization algorithm implemented by [25] has been adapted in order to simulate contact lines accurately. Moreover, contrary to [25], the high-order

operators of [2] are used to compute nodal $\nabla\phi_{\text{map}}$ and $\boldsymbol{n}_\Gamma$. For robustness issues, $\nabla\phi_{\text{map},ik}$ and $\boldsymbol{n}_{\Gamma,ik}$ in Eq (27) are evaluated at edge center from nodal $\nabla\phi_{\text{map}}$ and $\boldsymbol{n}_\Gamma$ using low order interpolation as in [25].

Remark 3. *The distance field used to compute $\boldsymbol{n}_\Gamma$ used in Eq. (27) is considered before the Blind Spot extensions described in 3.3.2. Using the normal after extension for re-initialization can lead to spurious interface creation, for low contact angle and highly curved interface close to the wall. Indeed, in this case the extended isocontours of distance can re-enter in the domain in the Blind Spot, leading to level-set creation during the re-initialization process.*

3.4.1. Wall treatment for re-initialization

Care must be taken for the discretization of the right-hand side of Eq. (27) on the boundaries and especially at walls. As a matter of fact, $\nabla\phi_{\text{map}}$ and $\boldsymbol{n}_\Gamma$ cannot directly be computed at nodes on the boundaries with the high-order differential operators due to a lack of neighbouring nodes (see [2] for more details). Consequently, $\nabla\phi_{\text{map},ik}$ and $\boldsymbol{n}_{\Gamma,ik}$ cannot be evaluated for edges containing at least one node on the wall. To tackle this problem and as proposed in [2], a Taylor series expansion is performed from the nodes one layer above the wall to the nodes on the wall with the equation

$$\nabla f_j = \nabla f_i + \nabla\nabla f_i \, \boldsymbol{\Delta}_{i,j} + \mathcal{O}\left(\Delta_{i,j}^2\right), \tag{28}$$

where f stands for ϕ or ϕ_{map}, i for the node index in the domain and j for the node index on the wall. After this operation, $\nabla\phi_{\text{map}}$ and $\boldsymbol{n}_\Gamma$ are correctly computed on the walls. This enables to evaluate accurately the right-hand side of Eq. (27) on nodes one layer above the wall. However, this correction is not enough to compute accurately the right-hand side of Eq. (27) for nodes on the wall. Indeed, the control volume decentering illustrated in Fig. 7 leads to an erroneous evaluation of the right-hand side of Eq. (27) for wall-nodes. To alleviate this problem, we directly apply the hyperbolic tangent profile for

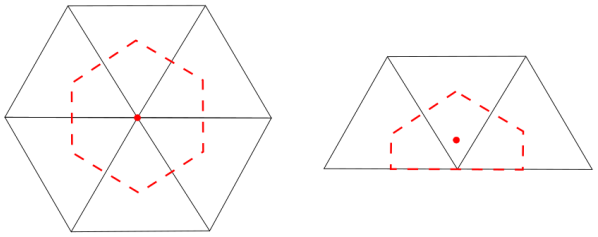

Figure 7: Control volume decentering for nodes on a boundary illustrated on a 2D regular mesh. Left: node in the domain. Right: node on a boundary. The control volume boundary is represented by the red dashed line and the control volume center, where the right-hand side of Eq. (27) is computed, by a red dot.

wall-nodes instead of solving Eq. (27)

$$\psi^{n+1} = \frac{1}{2}\left(\tanh\left(\frac{\phi^{\text{n}}}{2\varepsilon}\right) + 1\right) + \left(\psi_{adv}^{n+1} - \psi^n\right), \tag{29}$$

where ψ_{adv}^{n+1} stands for the level-set after advection at iteration $n+1$ and ϕ is the distance prior to extension in the Blind Spot, consistent with re-initialization in the rest of the domain. ϕ being known only at iteration n when re-initializing ψ (see the scheme of the overall algorithm on Fig. 9), the profile is corrected by the variation of ψ at iteration $n+1$ due to advection. Furthermore, the closest node to the contact line in the obtuse side of the contact angle is not re-initialized, i.e. $\psi^{n+1} = \psi_{adv}^{n+1}$. This methodology allows to build a hyperbolic tangent profile without moving the interface close to the wall during the re-initialization process.

As pointed out by Zahedi et al. [61] and Sato and Ničeno [49], it is essential that the flux of ψ is null through the walls, the interest of conservative level-set being lost otherwise. The non-penetration condition of the velocity naturally imposes a zero flux through the wall during advection. However, $\boldsymbol{n}_\Gamma$ being not always aligned with the wall, a flux of level-set can pass through the wall. To alleviate this, we adapted the method proposed by [49] to unstructured grid. The flux of level-set bewteen the nodes one layer above the wall and the nodes on the wall is imposed to zero by using the control volume tangential component of the normal $\boldsymbol{n}_{\Gamma,ik,||} = \boldsymbol{n}_{\Gamma,ik} - \left(\boldsymbol{n}_{\Gamma,ik} \cdot \frac{\mathbf{d}\boldsymbol{A}_{ik}}{||\mathbf{d}\boldsymbol{A}_{ik}||}\right) \frac{\mathbf{d}\boldsymbol{A}_{ik}}{||\mathbf{d}\boldsymbol{A}_{ik}||}$ instead of $\boldsymbol{n}_{\Gamma,ik}$ to evaluate $\boldsymbol{n}_{\Gamma,ik} \cdot \mathbf{d}\boldsymbol{A}_{ik}$ in Eq. (27).

The impact of our enhancements on the level-set re-initialization is illustrated on Fig. 8. A steady interface forms an angle $\theta_{eq} = 20°$ with wall. 50 pseudo-iterations of re-initialization are performed to accentuate the effect of re-initialization without advection. The isocontour $\psi = 0.5$ is shown in the contact

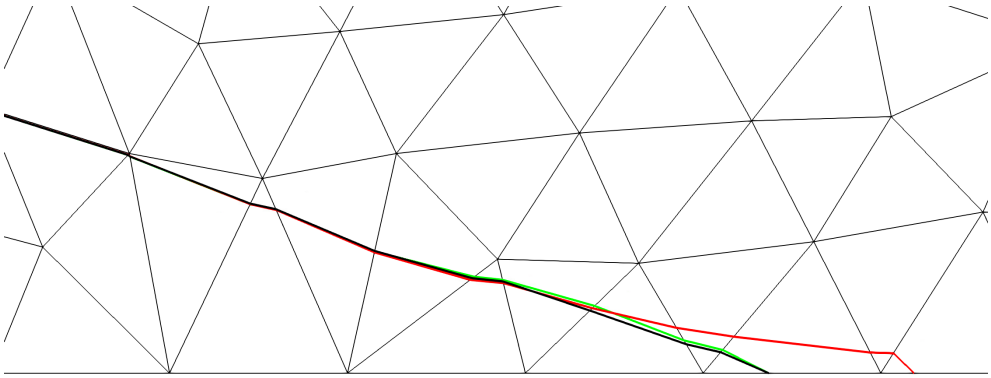

Figure 8: Effect of re-initialization at contact line. The interface before re-initialization is in black, the interface after the re-initialization of [25] is in red and the interface after the re-initialization proposed in this paper is in green.

line neighbourhood before re-initialization and after it, with the re-initialization of [25] and ours. It can be seen that the standard re-initialization moves the contact line while our version does not displace the interface close to the wall. The two methods show the same good accuracy far from the contact line.

Finally, despite not being fully conservative because of the non-conservative re-initialization at wall-nodes, the methodology presented in this work shows good conservation properties as illustrated in section 4.

3.5. Projection method for pressure-velocity coupling

In the YALES2 code, the original projection method of Chorin [8, 9] and Temam [55] is slightly modified to improve the accuracy of the velocity field [38]. A brief summary of this method is recalled here for clarity.

1. First, a velocity predictor $\boldsymbol{u}^*$ is explicitely computed with $\boldsymbol{u}^n$ and $P^{n-1/2}$ by solving

$$\frac{\boldsymbol{u}^* - \boldsymbol{u}^n}{\Delta t} = -\nabla \cdot (\boldsymbol{u}^n \otimes \boldsymbol{u}^n) - \frac{\nabla P^{n-1/2}}{\rho} + \frac{1}{\rho}\nabla \cdot \left(\mu \left(\nabla \boldsymbol{u}^n + (\nabla \boldsymbol{u}^n)^T\right)\right) + \boldsymbol{g}. \tag{30}$$

   This velocity field is *a priori* not divergence-free and has to be corrected to satisfy Eq. (1).

2. The velocity predictor is corrected with the new pressure field and the pressure contribution at previous iteration is removed, i.e.

$$\frac{\boldsymbol{u}^{n+1} - \boldsymbol{u}^*}{\Delta t} = -\frac{\nabla P^{n+1/2}}{\rho} + \frac{\nabla P^{n-1/2}}{\rho}. \tag{31}$$

   To solve Eq. (31), the new pressure field $P^{n+1/2}$ has to be known. Taking the divergence of Eq. (31) and enforcing $\nabla \cdot \boldsymbol{u}^{n+1} = 0$, we obtain the Poisson equation for the pressure

$$\nabla \cdot \left(\frac{\nabla P^{n+1/2}}{\rho}\right) = \frac{\nabla \cdot \boldsymbol{u}^*}{\Delta t} + \nabla \cdot \left(\frac{\nabla P^{n-1/2}}{\rho}\right). \tag{32}$$

   After discretization of the pressure laplacian, the resulting linear system is solved using a Deflated Preconditionned Conjugate Gradient (DPCG) solver [39]. The pressure gradient computed with the new pressure field is used to solve Eq. (31).

Additional details on the projection method applied to two-phase flows are given in Sahut et al. [48].

The temporal integration being explicit for all terms, the time step is computed at each iteration with

$$\Delta t = \min\left(\Delta t_{conv}, \Delta t_{visc}, \Delta t_{cap}\right), \tag{33}$$

where Δt_{conv}, Δt_{visc} and Δt_{cap} are the classical time step stability constraints corresponding respectively to convection, diffusion and surface tension [4].

3.6. Ghost-Fluid method

For two-phase flows, a special treatment has to be applied to discretize the pressure laplacian and gradient in the interface vicinity to take the pressure discontinuity Eq. (3) into account. To this purpose, the ghost fluid method is used to apply the pressure jump at the interface. With this method, $[P]_\Gamma$, defined only at the interface, is expanded to the interface closest nodes in both phases as follows, in order to use a ghost pressure for pressure laplacian and gradient computation. If $i+1$ is the index of the node in the liquid and i the index of the node in the gas, Desjardins et al. [15] derived an expression for the pressure jump in the liquid

$$[P]_{i+1} = \frac{\rho_g}{\rho_*}[P]_\Gamma + \left(1 - \frac{\rho_g}{\rho_*}\right)(P_{l,i+1} - P_{g,i}), \tag{34}$$

with

$$\rho_* = \rho_g\theta + \rho_l(1-\theta), \tag{35}$$

with the definition of θ given in Eq. (26). The gas ghost pressure at node $i+1$,

$$P_{i+1}^{g,ghost} = P_{i+1}^{l} - [P]_{i+1}, \tag{36}$$

is used to discretize the pressure laplacian to solve for P and then to compute the pressure gradient in a classic finite volume way to correct the velocity predictor into a divergence-free velocity field. The same procedure is used to compute the liquid ghost pressure.

In this study, it was found that for high density ratios (typically $\rho_l/\rho_g = 1000$), $[P]_{i+1}$ is highly dependent on the interface position at sub-grid level. This leads to unphysical fluctuations of the pressure field and therefore numerically unstable contact line dynamics. Even if less accurate at sub-grid level, it is more robust and less mesh dependent to consider the interface at the center of the edge between i and $i+1$ instead of using the sub-grid position θ. We write thus

$$[P]_{i+1} = \frac{\rho_g}{\overline{\rho}}[P]_\Gamma + \left(1 - \frac{\rho_g}{\overline{\rho}}\right)(P_{l,i+1} - P_{g,i}), \tag{37}$$

where

$$\overline{\rho} = \frac{\rho_g + \rho_l}{2}. \tag{38}$$

Further details on pressure laplacian discretization on multi-dimensional unstructured meshes with pressure jump imposition at interface are given in Sahut et al. [48].

Finally, the different steps of the proposed algorithm are summarized on Fig. 9.

4. Results

4.1. Equilibrium shape of a 2D drop on a flat wall

To assess the contact angle imposition method, a classic canonical 2D test case is performed [17, 57]. As illustrated on Fig. 10, a steady semicircular drop is initialized on a flat wall with an initial 90° contact angle. The imposed angle (constant and uniform) can differ from the initial angle. Due to surface tension and sub-grid scale curvature, the contact points move in order to respect the imposed contact angle. In order to assess only the contact angle imposition method, the Navier slip condition is replaced in this case by a free-slip condition at walls, i.e. $\left.\frac{\partial \boldsymbol{u}_{||}}{\partial y}\right|_{wall} = 0$. This enables to reach the equilibrium position faster, without possible artifacts due to the Navier slip condition discretization. Gravity being null, the equilibrium shape of the drop must be a circular cap. Using mass conservation, the radius R^{th}, the spreading length L^{th} and the height e^{th} of the equilibrium interface in function of the initial radius R_0 and the imposed contact angle θ_{eq} (in the liquid) can be derived

$$R^{th} = R_0\sqrt{\frac{\pi}{2\left(\theta_{eq} - \sin(\theta_{eq})\cos(\theta_{eq})\right)}}, \tag{39}$$

$$L^{th} = 2\,R^{th}\sin(\theta_{eq}), \tag{40}$$

$$e^{th} = R^{th}\left(1 - \cos(\theta_{eq})\right). \tag{41}$$

The physical parameters are taken from Wang and Desjardins [57] and summed-up in Table 3. The surface tension is deliberately small to minimize capillary waves generated by the discrepancy between the initial and the imposed contact angle. As in [57], the spreading length and the height of the equilibrium drop are compared to the theoretical value to assess the accuracy of the contact angle imposition. The

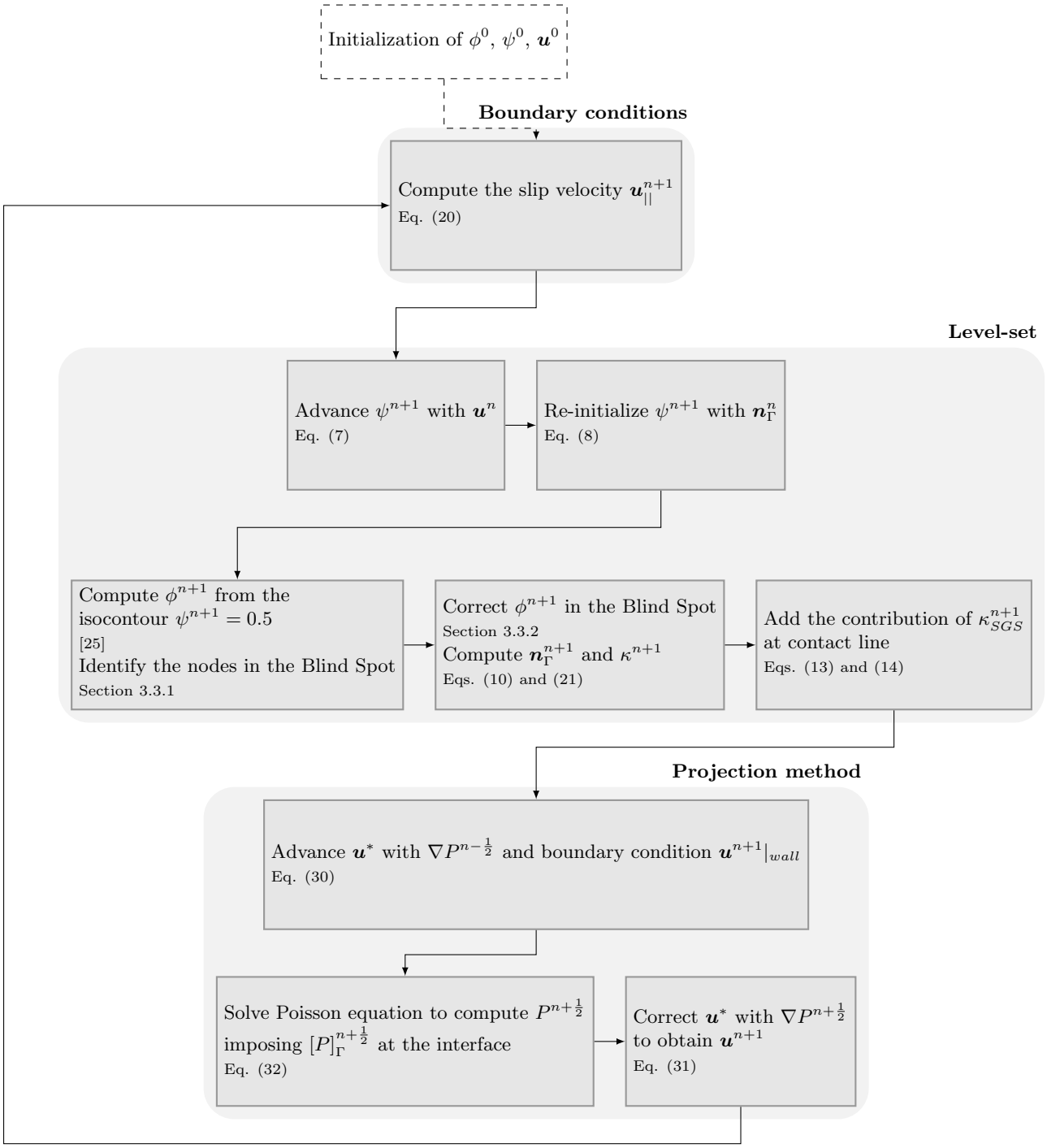

Figure 9: Main steps of the algorithm used in the solver presented in this paper.

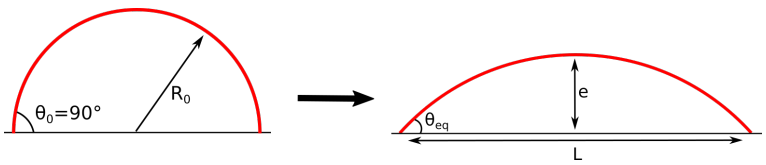

Figure 10: 2D contact angle imposition test case. Left: initial condition, right: equilibrium solution.

Drop radius	R_0	0.01 m
Gas density	ρ_g	1 kg.m^{-3}
Liquid density	ρ_l	1000 kg.m^{-3}
Gas viscosity	μ_g	10^{-5} kg.s^{-1}.m^{-1}
Liquid viscosity	μ_l	10^{-2} kg.s^{-1}.m^{-1}
Surface tension	σ	10^{-5} N.m^{-1}

Table 3: Parameters for 2D drop equilibrium on a flat wall.

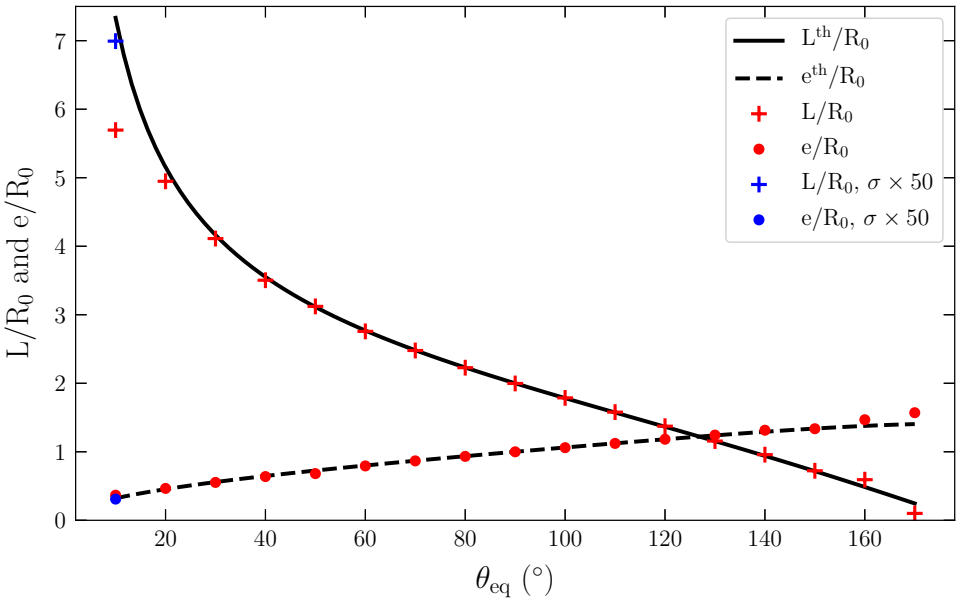

Figure 11: Normalized spreading length L/R_0 and normalized height e/R_0 at equilibrium as a function of the imposed contact angle θ_{eq}. The blue symbols show the effect of an increased surface tension.

imposed angles vary from 10° to 170° with increment of 10°. The mesh is an unstructured triangular grid with an average cell size $\overline{\Delta}$ such as $R_0/\overline{\Delta} = 20$. The normalized spreading lengths and heights are plotted on Fig. 11 as a function of the imposed contact angle. The results show a rather good agreement with the analytical solution. For the lowest contact angle, the computed spreading length differs from the analytical solution, as observed in [57]. This is however not the case for the drop height. This discrepancy can be explained by the fact that for low contact angles, the distance to be travelled by the contact line is higher than for high contact angles. So, by the time the drop approaches its equilibrium state, the initial momentum imparted to the liquid by the out-of-equilibrium contact angle has been dissipated by viscous effects, and the resulting late-stage dynamics is relatively weak. Thus, when the current contact angle value is close to the imposed contact angle value, the contact angle imposition force can be counterbalanced by spurious currents or level-set re-initialization effects. If the surface tension coefficient is increased, the spreading length at equilibrium gets closer to the theoretical prediction as illustrated by the blue symbols on Fig. 11.

For the contact angle $\theta_{eq} = 45°$ we perform a mesh convergence for grid sizes corresponding to $R_0/\overline{\Delta} \in [2.5\,;\,80]$. The drop height error and the spreading length error are represented in Table 4. No

$R_0/\overline{\Delta}$	2.5	5	10	20	40	80
$\lvert \mathrm{L^{th}} - \mathrm{L} \rvert / \mathrm{L^{th}}$	1.38%	1.49%	0.42%	0.02%	0.10%	0.23%
$\lvert \mathrm{e^{th}} - \mathrm{e} \rvert / \mathrm{e^{th}}$	2.44%	1.44%	0.06%	0.34%	0.02%	0.35%

Table 4: Normalized spreading length error and normalized drop height error at equilibrium for different mesh resolutions in 2D. The imposed contact angle is $\theta_{eq} = 45°$.

clear convergence with mesh refinement is observed for both quantities. Nevertheless we draw the reader's attention to the fact that the errors remain under 1% for fine meshes, which is considered satisfactory for our applications. A likely explanation for the non-convergence can be found in the curvature computation which does not converge at contact line when computed on a second-order level-set field as shown in section 3.3.3.

4.2. Equilibrium shape of a 3D drop on a flat wall

The case of the previous section is now adapted to 3D. A steady hemispherical drop is initialized on a flat wall with an initial 90° contact angle. The equilibrium drop shape is given by [49]

$$R^{th} = R_0 \left(\frac{2}{\left(1 - \cos\left(\theta_{eq}\right)\right)\left(1 + \sin^2\left(\theta_{eq}\right) - \cos\left(\theta_{eq}\right)\right)} \right)^{\frac{1}{3}}, \tag{42}$$

$$L^{th} = 2\,R^{th} \sin\left(\theta_{eq}\right), \tag{43}$$

$$e^{th} = R^{th}\left(1 - \cos\left(\theta_{eq}\right)\right), \tag{44}$$

with the same notations as in previous section. The contact line radius is $r_{CL}^{th} = L^{th}/2$. The initial radius R_0 and the physical properties are identical as the 2D case and are given in Table 3. A free-slip condition is applied on the wall. A mesh convergence study is performed for the contact angle $\theta_{eq} = 45°$ on four meshes. A slice of the interface is represented at initialization and at equilibrium on Fig. 12. The relative

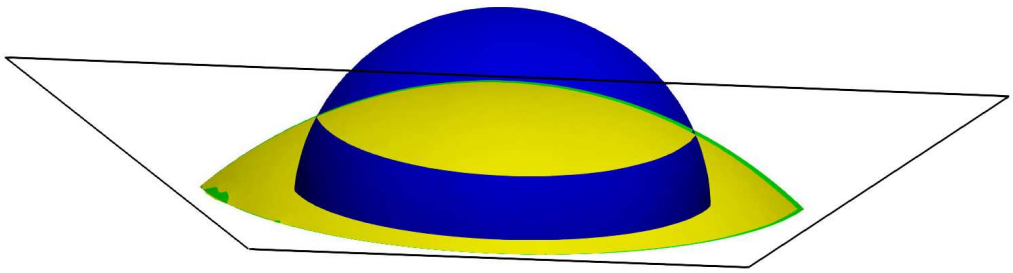

Figure 12: Vertical slices of the drop for a contact angle $\theta_{eq} = 45°$ on a mesh such that $R_0/\overline{\Delta} = 10$. The view is taken from below the wall which is represented by the black line. The initial drop (blue) and the drop at equilibrium are represented (yellow: computed, green: theoretical).

errors are defined as

$$L^{\infty}(r_{CL}) = \frac{1}{r_{CL}^{th}} \max_{ik \in N_{CL}} |r_{CL}^{th} - r_{CL}^{ik}|, \tag{45}$$

$$L^{2}(r_{CL}) = \frac{1}{r_{CL}^{th}} \sqrt{\frac{1}{N_{CL}} \sum_{ik=1}^{N_{CL}} \left(r_{CL}^{th} - r_{CL}^{ik}\right)^2}, \tag{46}$$

$$L^{\infty}(e) = \frac{1}{e^{th}} |e^{th} - \max_{ik \in N_{\Gamma}} e^{ik}|, \tag{47}$$

$$\tag{48}$$

with r_{CL}^{ik} the computed contact line radius at edge ik crossed by the contact line, N_{CL} the number of edges crossed by the contact line, e^{ik} the computed interface height above the wall at edge ik crossed by the interface and N_{Γ} the number of edges crossed by the interface. The errors are gathered in Table 5. Contrary to the 2D case, all errors are converging with mesh refinement at an order bewteen 1 and 2.

$R_0/\overline{\Delta}$	2.5	5	10	20
$L^{\infty}(r_{CL})$	33.28%	8.06%	4.18%	1.42%
$L^{2}(r_{CL})$	22.32%	3.35%	1.22%	0.47%
$L^{\infty}(e)$	15.86%	4.45%	1.85%	0.65%

Table 5: Normalized contact line radius error and normalized drop height error at equilibrium for different mesh resolutions in 3D. The imposed contact angle is $\theta_{eq} = 45°$.

Even if the curvature computation suffers from the same limitations as in 2D, the 3D case has the benefit that a local spurious contact line blocking can be overcome by the overall contact line inertia, resulting in a smoother dynamics and less dependency on local errors. This is an interesting point since the developed methodology is devoted to simulate contact lines on 3D realistic geometries. It can be noticed that the error magnitudes are higher in 3D than in 2D for a same characteristic cell size. The error magnitudes are however considered small enough for fine meshes.

4.3. 2D capillary rise with Navier slip boundary condition

The contact angle implementation being validated, we now turn to a more complex case including dynamics with a Navier slip condition at wall. Gründing et al. [21] have extensively simulated the rise and oscillations of a meniscus in a 2D capillary for various rise regimes and slip lengths, using different interface tracking/capturing methods. Capillary rise happens when a straw is introduced in a steady bath of hydrophilic liquid. The set up consists in a 2D vertical capillary with gravity pointing downward. The capillary half-width is noted R. Constant pressure boundary conditions are applied at the bottom and the top such that $P_{top} = P_{bottom} = 0$. The bottom of the capillary is thus supposed at the height of the free surface of the bath. The liquid-gas interface is initialized as a steady meniscus respecting the contact angle θ_{eq} at the wall, which is imposed all along the simulation. The meniscus equilibrium height above the capillary basis is given by Jurin [26] with the expression

$$h_{Jurin}^{2D} = \frac{\sigma \cos(\theta_{eq})}{R \rho_l g}, \tag{49}$$

which is the balance between capillary force and gravity. In Eq. (49) the meniscus height is supposed constant across the capillary section. If the interface is a circular section, the meniscus apex height has been derived by [21] and is given by

$$h_{apex} = h_{Jurin}^{2D} - \frac{R}{2\cos(\theta_{eq})} \left(2 - \sin(\theta_{eq}) - \frac{\arcsin(\cos(\theta_{eq}))}{\cos(\theta_{eq})}\right) \tag{50}$$

The initial meniscus apex height is set to the arbitrary value $h_{apex}^{0} = 2R$ and the relation $h_{Jurin}^{2D} = 4R$ is verified for all the simulations. The transient phase is ruled by the dimensionless number [21]

$$\Omega = \sqrt{\frac{9\sigma \cos(\theta_{eq}) \mu_l^2}{\rho_l^3 g^2 R^5}}. \tag{51}$$

Using a simplified model for the capillary rise, the authors in [21] proved that oscillations are observed for $\Omega < 2$. We focus on this regime in this study. As in [21], two slip length values for the Navier slip

Ω -	R [m]	ρ_l [kg.m^{-3}]	ρ_g [kg.m^{-3}]	μ_l [kg.s^{-1}.m^{-1}]	μ_g [kg.s^{-1}.m^{-1}]	g [m.s^{-2}]	σ [N.m^{-1}]	θ_{eq} [°]
0.1	0.005	1663.8	1.6638	0.01	0.00001	1.04	0.2	30
1	0.005	83.1	0.0831	0.01	0.00001	4.17	0.04	30

Table 6: Parameters for 2D capillary rise.

condition have been used, namely $\lambda = R/5$ and $\lambda = R/50$. The aim is not to represent a realistic slip, which happens at nanometer scale, but to assess the Navier slip condition implementation and its effect on the meniscus oscillations. The physical properties are summed-up in Table 6. Only half of the capillary is simulated thanks to a planar symmetry condition applied along the capillary center. The height of the domain is set to $h_D = 12R$. The simulations are performed on three levels of mesh refinement given by the characteristic cell size $\overline{\Delta} = R/10,\ R/20,\ R/40$. The initial condition is shown on Fig. 13 on the coarsest mesh. A time convergence study detailed in AppendixC has shown that the time step computed

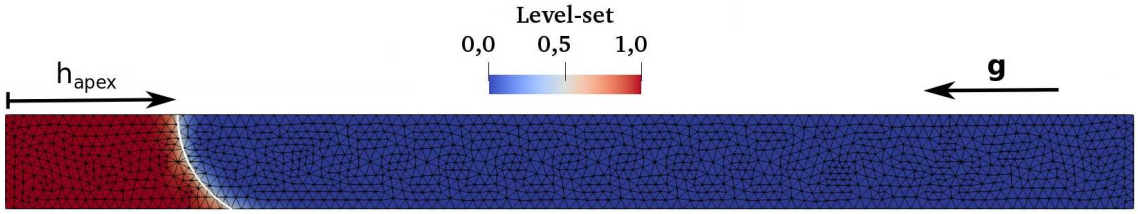

Figure 13: Domain for simulation of the capillary rise. The initial level-set field is displayed and the interface is represented in white. Gravity points leftward.

with stability constraint Eq. (33) is small enough to consider the time discretization errors negligible compared to space discretization errors. The results of [21] obtained with a geometric Volume of Fluid method on a fine grid defined by $\overline{\Delta} = R/128$ are considered as a reference and are compared with ours.

First, the case with $\Omega = 1$ is simulated for both slip lengths. The meniscus apex height is plotted against time on Fig. 14 for the three levels of mesh refinement. The slip length has an important effect

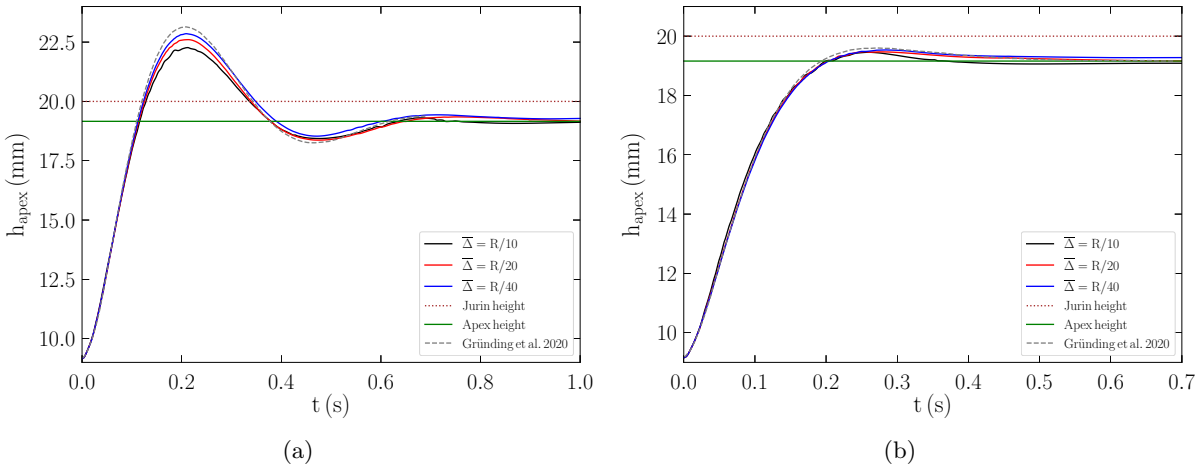

Figure 14: Height of meniscus apex evolution versus time with $\Omega = 1$ on three grids. (a) $\lambda = R/5$. (b) $\lambda = R/50$.

on the dynamics of the meniscus. For the small slip length, almost no oscillations are observed. A good agreement with the results of [21] is found for both slip lengths and all results converge at stationnary state toward the theoretical apex height predicted by Eq. (50). Refining the mesh enables to decrease the discrepancy between our results and those of [21], especially for the most oscillatory case.

The case with $\Omega = 0.1$ is now simulated, only for $\lambda = R/5$. The mesh study is shown on Fig. 15. Compared to Fig. 14a, the amplitude of the oscillations is much higher, revealing the strong impact of Ω on the transient behaviour of the meniscus. Once again, all results converge toward the theoretical prediction at equilibrium. A good mesh convergence toward the results of [21] is also observed. It can be noticed that the coarser the mesh is, the faster the oscillations are damped. This is likely caused by higher numerical diffusion on coarse grids.

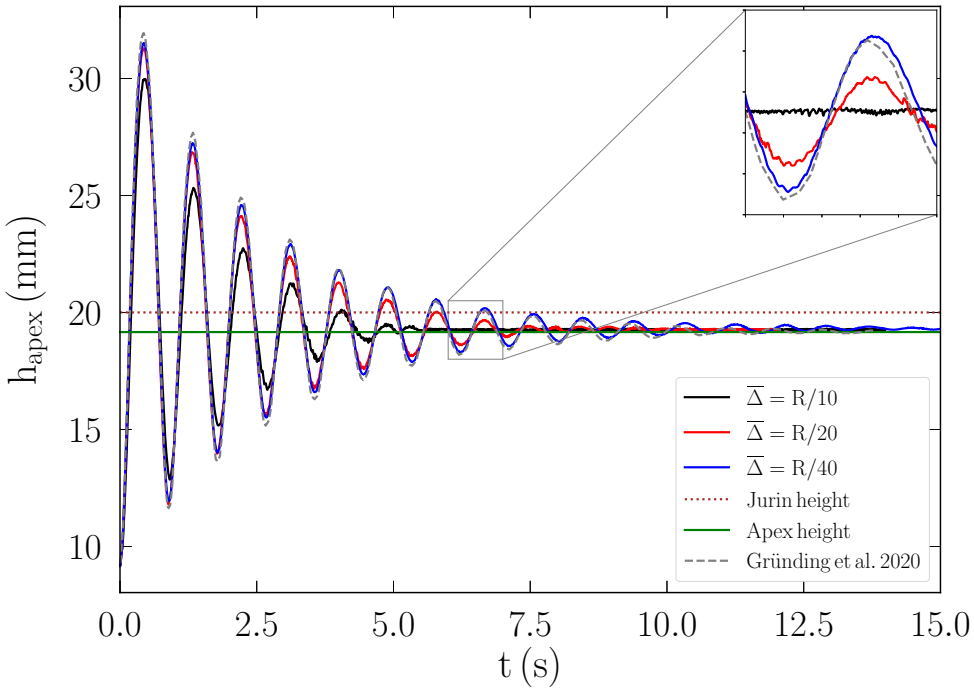

Figure 15: Height of meniscus apex evolution versus time with $\Omega = 0.1$ on three grids.

These manufactured cases have enabled to validate successfully the Navier slip boundary condition on two-phase flows with contact angle imposition. The developed methodology can therefore be employed to simulate realistic contact line simulations.

4.4. Drop impact on a sphere

Another test case, designed by Wang and Desjardins [57], is performed to evaluate the numerical method robustness and mass conservation on complex geometries. No analytical solution is known for this case. A 3D drop impact on a solid sphere is simulated for several wettabilities. The initial drop diameter d_d is equal to the solid sphere diameter d_s. The initial gap between the drop and the solid sphere is $d_s/4$ and the initial velocity of the drop is u_0. We consider the same physical parameters as in [57], listed in Table 7. The mesh is such that $R_0/\overline{\Delta} = 12.5$. Depending on the contact angle, the dynamic

Diameter ratio	d_d/d_s	1
Density ratio	ρ_l/ρ_g	1000
Viscosity ratio	μ_l/μ_g	100
Reynolds number	$\rho_l u_0 d_d/\mu_l$	50
Weber number	$\rho_l u_0^2 d_d/\sigma$	2.5

Table 7: Parameters for drop impact on a solid sphere.

response of the drop can differ significantly. The impact dynamics for $\theta_{eq} = 10°$ is illustrated on Fig. 16. After a spreading phase, the drop reaches an equilibrium position on the sphere with a low contact angle. The spreading dynamics appears to be slightly slower than in [57] and contrary to that study the solid is not fully wetted by the liquid at the final steady state. This different behaviour at equilibrium position can be explained by the different wall velocity condition between both studies: numerical slip due to no-slip discretization in [57] and Navier slip condition with resolved slip length in our case. As discussed in section 2.4, this can have a strong influence on the spreading dynamics. Fig. 17 describes the impact dynamics for $\theta_{eq} = 150°$. The drop does not spread on the hydrophobic sphere and finally bounces back from the solid. The equilibrium positions of the drops for different wettabilities are gathered on Fig. 18. The local contact angle is measured with $\theta_{me} = \cos^{-1}\left(-\boldsymbol{n}_{\Gamma,CL} \cdot \boldsymbol{n}_{wall,CL}\right)$. This local angle is then averaged on the whole contact line. The drop bounces back for the two most hydrophobic cases, i.e. $\theta_{eq} = 150°, 170°$. Except for the lowest angle, the contact angle imposition is performed with good

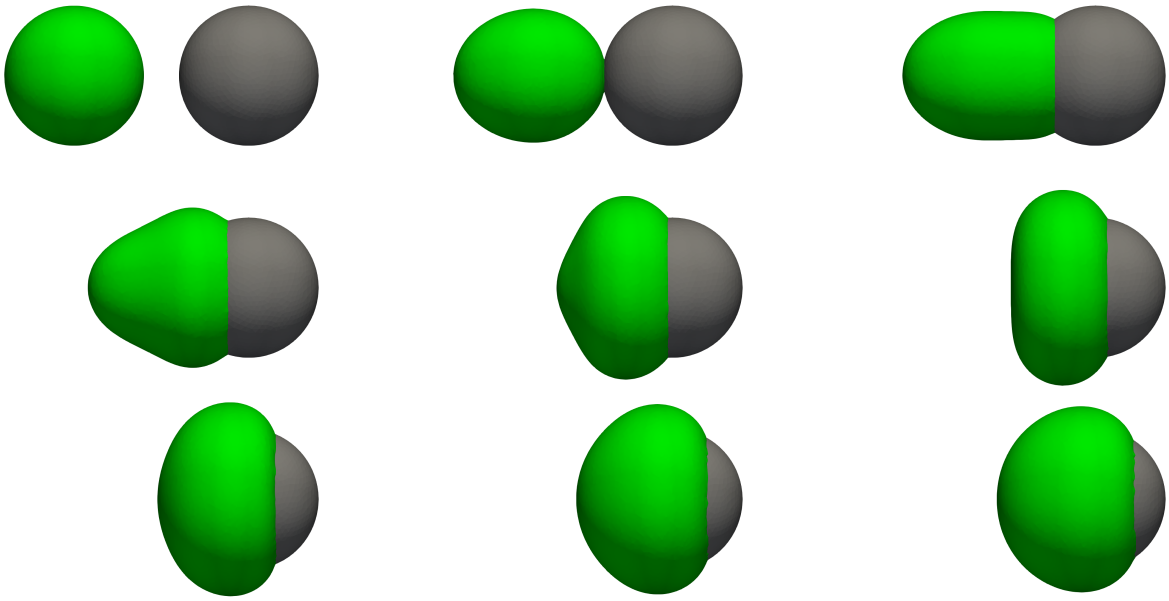

Figure 16: Time evolution of the drop impact on a hydrophilic sphere with $\theta_{eq} = 10°$. The dimensionless time interval between two successive pictures is $\Delta t u_0/d_d = 0.25$ (from left to right and from top to bottom).

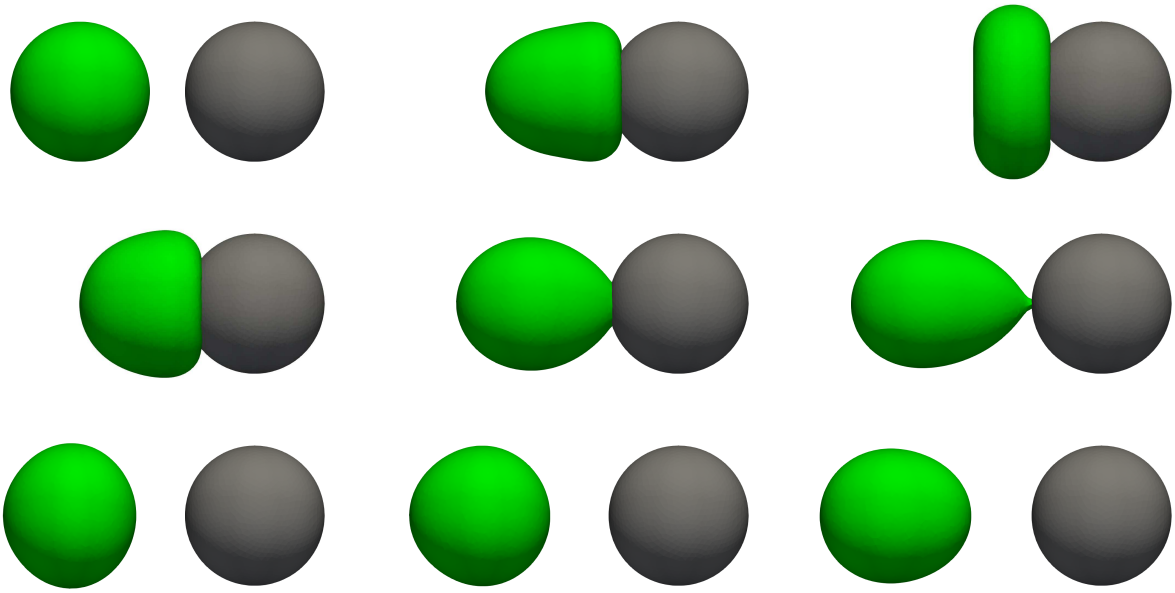

Figure 17: Time evolution of the drop impact on a hydrophobic sphere with $\theta_{eq} = 150°$. The dimensionless time interval between two successive pictures is $\Delta t u_0/d_d = 0.5$ (from left to right and from top to bottom).

$\theta_{eq} = 10°$ $\overline{\theta}_{me} = 4°$ | $\theta_{eq} = 30°$ $\overline{\theta}_{me} = 26°$ | $\theta_{eq} = 60°$ $\overline{\theta}_{me} = 59°$ | $\theta_{eq} = 90°$ $\overline{\theta}_{me} = 90°$ | $\theta_{eq} = 120°$ $\overline{\theta}_{me} = 119°$ | $\theta_{eq} = 150°$ $\overline{\theta}_{me} = -$ | $\theta_{eq} = 170°$ $\overline{\theta}_{me} = -$

Figure 18: Equilibrium positions of the drops for various contact angles. The imposed contact angle θ_{eq} and the effectively measured average contact angle $\overline{\theta}_{me}$ are written below the corresponding drop. The snapshots are taken at dimensionless time $\Delta t u_0/d_d = 10$.

accuracy as illustrated by the contact angle measurements. The code is robust for all cases: no parameter has been adjusted from a simulation to the other in order to ensure stability. The normalized error on liquid mass conservation is plotted against the dimensionless time on Fig. 19. The error remains almost always below 2% which we consider satisfactory for such geometry and unstructured mesh.

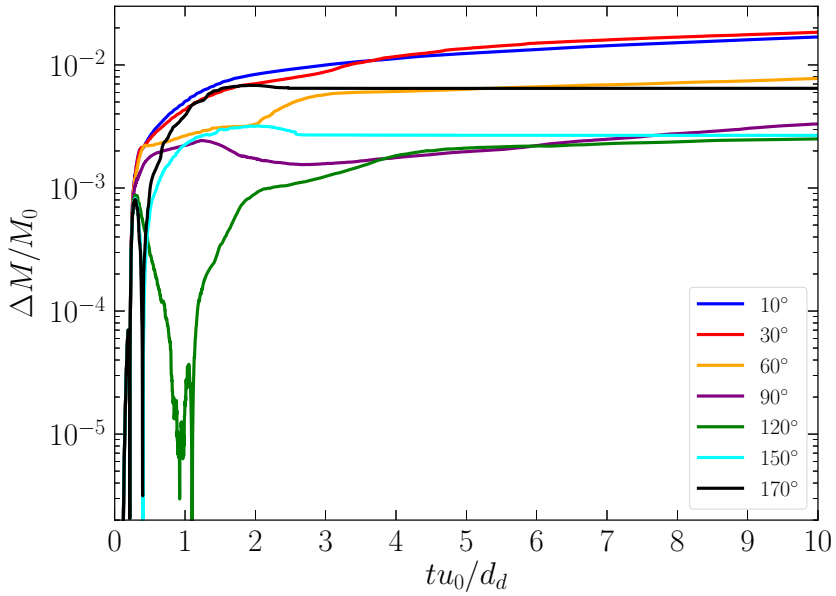

Figure 19: Error on mass conservation normalized by the initial drop mass M_0 versus dimensionless time for a drop impact on a sphere for various wettabilities.

4.5. Dynamics of a 3D drop spreading on a flat wall

In this section, the contact line dynamics is studied through the spontaneous spreading of a spherical 3D drop initially barely touching a flat wall. The main behaviours of the contact line with time are summarized by Wang and Desjardins [57]. During the initial phase of the spreading, known as inertial spreading, the contact line radius grows as $r_{CL} \sim t^{1/2}$, independently of the wettability [58]. At the end of the spreading, known as viscous spreading, the contact line radius follows Tanner's law given by $r_{CL} \sim t^{1/10}$ for total wetting and small droplets, i.e. when gravity can be neglected [54, 10, 11]. The duration of the inertial regime was derived by Biance et al. [3] and is defined as

$$t_{in} \sim \left(\frac{\rho_l \sigma R_0}{\mu_l^2}\right)^{1/8} \sqrt{\frac{\rho_l R_0^3}{\sigma}}, \tag{52}$$

where R_0 is the initial drop radius. Due to the power 1/8, the inertial regime duration can be approximated by the inertial/capillary time scale of the drop which gives $t_{in} \sim \sqrt{\rho_l R_0^3/\sigma}$.

We propose to validate our method against these observations by simulating the spreading of a viscous drop on a hydrophilic wall defined by $\theta_{eq} = 10°$ or $30°$. The physical parameters are identical to [57] and listed in Table 8. The inertial/capillary time scale is $\sqrt{\rho_l R_0^3/\sigma} \simeq 4.874$ ms. Gravity is not considered. A

Drop radius	R_0	1 mm
Gas density	ρ_g	1 kg.m^{-3}
Liquid density	ρ_l	974 kg.m^{-3}
Gas viscosity	μ_g	1.8×10^{-5} kg.s^{-1}.m^{-1}
Liquid viscosity	μ_l	62.2×10^{-3} kg.s^{-1}.m^{-1}
Surface tension	σ	0.041 N.m^{-1}

Table 8: Parameters for 3D drop spreading on a flat wall.

steady spherical drop is initialized with its center at $L = 0.98R_0$ above the wall. The initial contact area

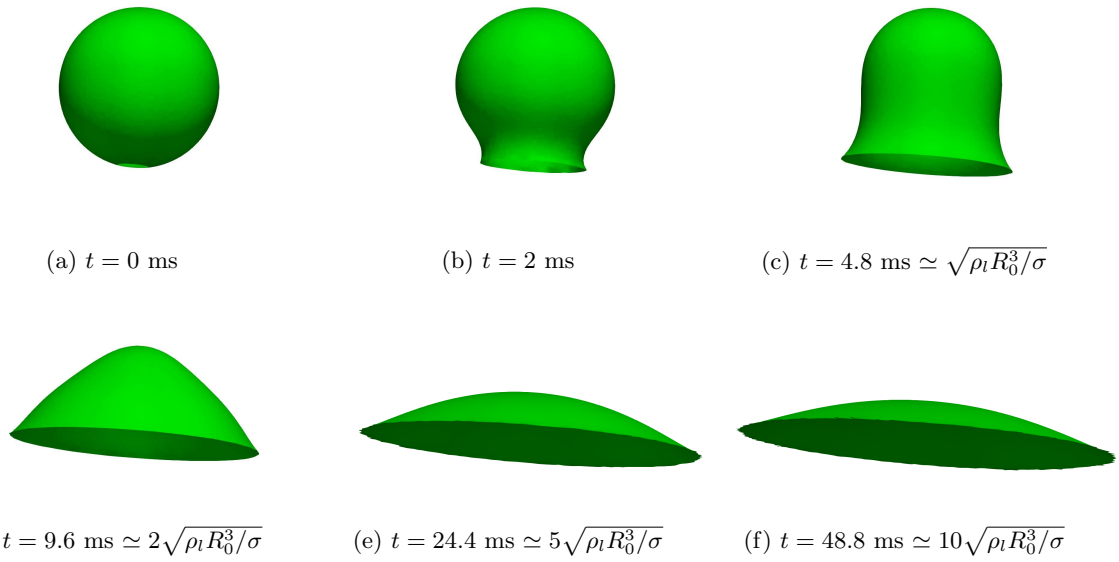

(a) $t = 0$ ms (b) $t = 2$ ms (c) $t = 4.8$ ms $\simeq \sqrt{\rho_l R_0^3/\sigma}$

(d) $t = 9.6$ ms $\simeq 2\sqrt{\rho_l R_0^3/\sigma}$ (e) $t = 24.4$ ms $\simeq 5\sqrt{\rho_l R_0^3/\sigma}$ (f) $t = 48.8$ ms $\simeq 10\sqrt{\rho_l R_0^3/\sigma}$

Figure 20: Time evolution of the drop shape during spreading on a flat surface with $\theta_{eq} = 10°$.

is thus a small disk. The dimensionless grid size is $R_0/\overline{\Delta} = 12.5$. The drop shape is shown at different instants of the spreading for $\theta_{eq} = 10°$ on Fig. 20. The contact line equivalent radius is computed as

$$r_{CL}(t) = \left(\frac{\int\limits_{wall} \psi(\boldsymbol{x}, t)\, \mathrm{d}S}{\pi} \right)^{1/2}, \tag{53}$$

where the wall integral of the level-set approximates the wetted area. We plot the normalized contact line radius r_{CL}/R_0 versus the normalized time $t/\sqrt{\rho_l R_0^3/\sigma}$ in log-log scale on Fig. 21. Our results are compared with those of Wang and Desjardins [57]. In addition, the initial theoretical contact line radius and the equilibrium contact line radii are plotted. As expected, at the beginning of the spreading the contact line radius grows roughly as $r_{CL} \sim t^{1/2}$ whatever the wettability. The inertial spreading lasts about twice the inertial/capillary time scale. This result is consistent with the theoretical prediction of [3]. The case with $\theta_{eq} = 10°$ is found to be the only one following Tanner's law as observed by [57]. For $\theta_{eq} = 30°$, the wettability is not high enough to follow Tanner's law, as expected [57, 3]. We remark that our results are similar to those obtained by Wang and Desjardins [57]. Both methods slightly overestimate the initial radius, by 44 % (ours) and 88 % ([57]), as one may expect given the few mesh elements on the contact area at initialization. Furthermore, we underline the fact that the computed radii get close to their theoretical equilibrium values at the end of the simulation. The proposed numerical method is thus able to reproduce the qualitative behaviour of a spreading drop on a flat wall, and quantitatively respects the expected scalings predicted by analytical models. To supplement these observations, the drop impact on a flat wall is compared with the experimental results of Šikalo et al. [50] in AppendixD. A good agreement is found for the inertial spreading while the later stage of the spreading exhibits discrepancies with experimental results. For better accuracy on this phase dominated by wettability effects, dynamic contact angle modelling could be helpful. It would allow to take into account the underresolved phenomena in the contact line vicinity. This is however beyond the scope of this paper.

4.6. Drop detachment from a fiber using dynamic mesh adaptation

In this section, our numerical method is employed to simulate the interaction between one or several drops and a fiber. The unstructured mesh is fitting the solid boundary, providing good accuracy of the flow close to the wall. Because of the changes of interface topology and important displacements of the liquid, using a uniformly fine mesh would require a tremendous number of cells. To avoid high computational time, a dynamic mesh adaptation algorithm developed by Leparoux et al. [31] and initially designed to study primary atomization is used. The number of cells is thus kept moderate with uniform and fine cells around the interface and large cells far away from the interface. This methodology ensures that the hyperbolic tangent profile of the level-set is discretized on uniform cell size distribution, preventing from large mass conservation issues. Moreover, the interface always crosses cells of the same size while it is advanced. This avoids numerical errors in the finite volume schemes for level-set advection Eq. (7) and re-initialization Eq. (8).

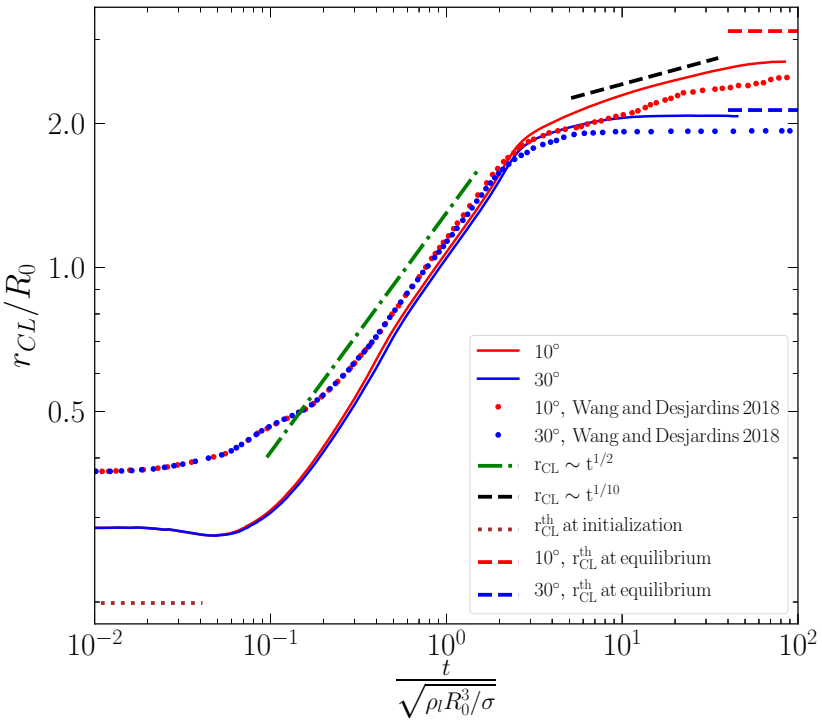

Figure 21: Contact line radius versus time during the spreading of a 3D drop for two different contact angles.

We consider in the two following sections drop interactions with a horizontal cylindrical fiber. In the first case, a pending drop is possibly detached from the fiber by gravity while in the second case two drops coalesce on the fiber and the release of surface energy generates their detachment.

4.6.1. Gravity-driven detachment from a horizontal fiber

The critical size of a drop hanging on a horizontal hydrophilic fiber and subjected to gravity has been studied experimentally and theoretically by Lorenceau et al. [36] and numerically by Wang and Desjardins [57]. Two forces are in competition: the weight of the drop and the wall adhesion force due to surface tension. When the drop reaches a critical size, the two forces cannot balance anymore and the drop eventually detaches from the fiber. As summed-up by [57] from the experimental results of [36], the critical drop radius can be computed as

$$R_c = \begin{cases} 1.65\kappa^{-1} & \text{if } R_f > \kappa^{-1} \\ 1.53 R_f^{1/3}\kappa^{-2/3} & \text{if } R_f < \kappa^{-1} \end{cases} \tag{54}$$

where R_f is the fiber radius and $\kappa^{-1} = \sqrt{\sigma/(\rho_l g)}$ is the capillary length. When the fiber radius is larger than the capillary length, the critical radius depends only on the fluid properties because the drop behaves as if it was hanging to a flat surface. Indeed, the fiber curvature is low compared to the drop curvature [36].

We perform simulations on unstructured grids to reproduce the results obtained by Wang and Desjardins [57] on cartesian grids. The physical parameters are enumerated in Table 9. The capillary length is thus $\kappa^{-1} \simeq 1.5$ mm, corresponding to a silicon oil. The liquid totally wets the fiber, which is approximated by a contact angle $\theta_{eq} = 10°$. For all the following simulations the fiber radius is smaller than the capillary length. We aim to determine the critical drop radius for four different fiber radii, defined by $R_f = 80$ µm, 175 µm, 350 µm and 700 µm. Various sizes of drops are simulated for each fiber. The drop is initialized as a steady sphere of radius R_d centered on the fiber as illustrated on Fig. 22. The meshes are such that $R_f/\overline{\Delta} = 2.5$ for $R_f = 80$ µm, $R_f/\overline{\Delta} = 4$ for $R_f = 175$, 350 µm and $R_f/\overline{\Delta} = 8$ for $R_f = 700$ µm. $\overline{\Delta}$ is the average cell size close to the interface. Fig. 23 shows the drops at equilibrium with initial radii from 400 µm to 1100 µm on a fiber of radius $R_f = 175$ µm. The upper images are from simulations of [57] and the lower images are the results obtained in this paper. The measured average contact angle $\overline{\theta}_{me}$ is written below each drop for those remaining attached to the fiber. In our simulations, the two largest drops detach from the fiber whereas only the largest drop falls in [57]. This discrepancy will be

Gas density	ρ_g	1 kg.m^{-3}
Liquid density	ρ_l	971 kg.m^{-3}
Gas viscosity	μ_g	1×10^{-5} kg.s^{-1}.m^{-1}
Liquid viscosity	μ_l	1×10^{-3} kg.s^{-1}.m^{-1}
Surface tension	σ	0.0214 N.m^{-1}
Gravitationnal acceleration	g	9.8 m.s^{-2}
Contact angle	θ_{eq}	10°

Table 9: Parameters for gravity-driven detachment from a horizontal hydrophilic fiber.

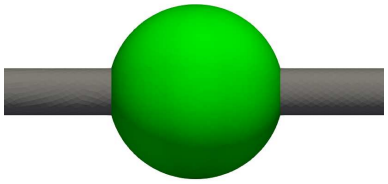

Figure 22: Drop initialization on a horizontal fiber. Gravity points downward.

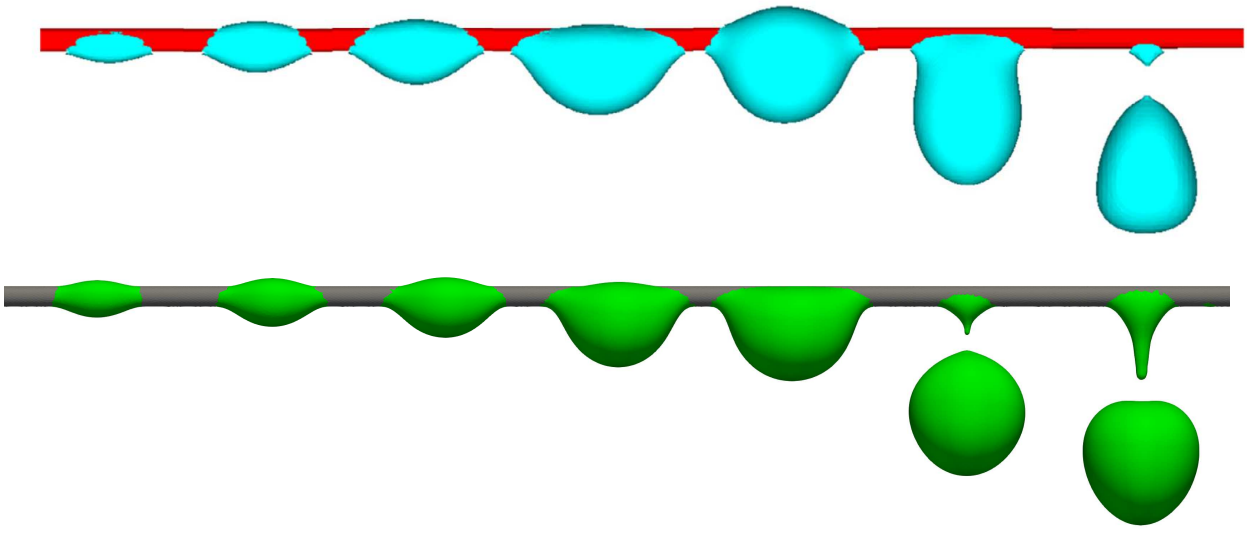

$\overline{\theta}_{me} = 4.6°$ $\overline{\theta}_{me} = 6.8°$ $\overline{\theta}_{me} = 7.0°$ $\overline{\theta}_{me} = 7.2°$ $\overline{\theta}_{me} = 6.7°$ – –

Figure 23: Equilibrium positions of different drops on a fiber with radius $R_f = 175$ µm. The initial drop radii are 400, 500, 600, 800, 900, 1000 and 1100 µm (from left to right). The upper images are from [57] and the lower images are from the current simulations. The average contact angle $\overline{\theta}_{me}$ measured on simulation results is written below the drops.

quantified further. In the other cases, the drops spread on the fiber and reach an equilibrium position. The drop shapes are similar between both studies. No analytical model is available to compare with.

The detachment dynamics is illustrated on Fig. 24 for a drop with an initial radius slightly above the critical radius. The fiber radius is $R_f = 350$ µm. The upper images are from the experiments of [36], the middle images are from the simulations of [57] and the lower images are the numerical results of this study. The drop initial radius is $R_d = 1300$ µm in this study. However, neither the initial radius nor the initial volume are specified in the two previous studies, hampering a quantitative comparison. The time interval between two successive pictures is 1 ms. The first snapshot of our simulation is taken at 55 ms after initialization of a spherical drop centered on the fiber. The authors of [57] do not give this information and the experiments in [36] are initialized differently, as explained below. The last snapshots are approximately synchronized between three studies. Even if the drop detachment

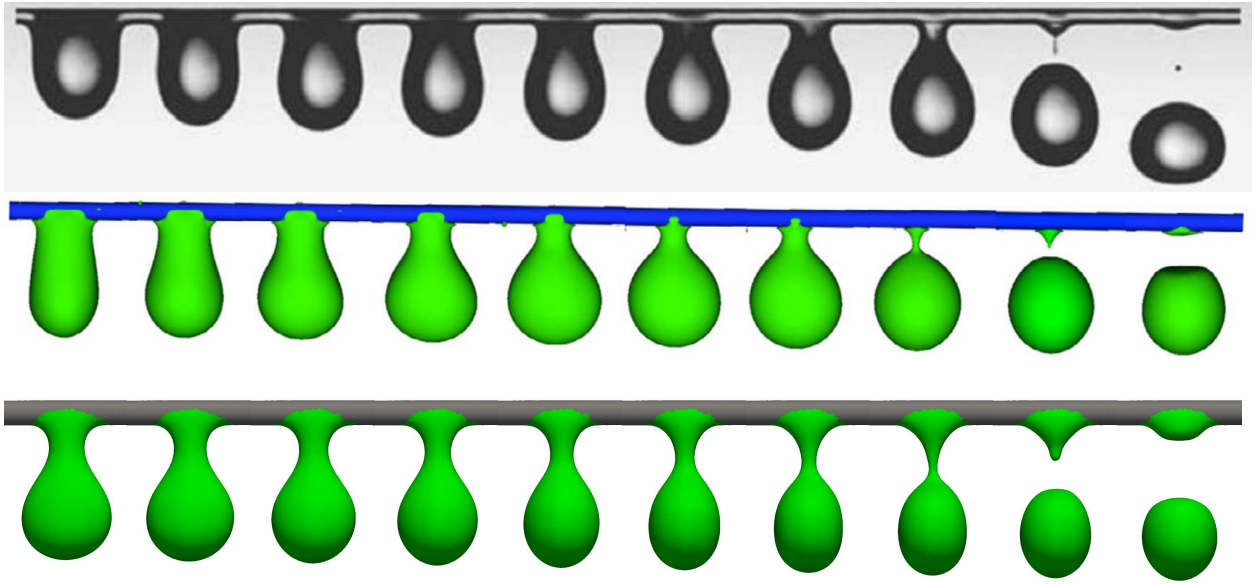

Figure 24: Snapshots of the drop detachment from a fiber with $R_f = 350$ µm. The upper images are from [36], the middle images are from [57] and the lower images are our result. The time interval between each snapshot is 1 ms (time elapses from left to right). Initial conditions are unknown for [36] and [57]. See the text at the end of section 4.6.1 for more details on the influence of initial conditions.

is qualitatively similar between the three studies, i.e. pinching of the filament and small amount of liquid remaining suspended to the lower part of the fiber, the detachment dynamics is rather different. The detachment appears to be faster in the experimental study of [36] than in both numerical studies. Moreover, the detachment is slower in our study than in [57]. This difference might be explained by the drop initialization: in the experimental study small droplets are gently added on the fiber until the resulting drop falls, while in our study the drop is directly set as a sphere centered on the fiber. The initialization is not detailed in [57]. The difference in the exact initial liquid mass might be another reason for the discrepancy. Indeed, the initial drop radius is not known for the results of the previous studies shown in Fig. 24. Our numerical experiment was run on a $R_f/\overline{\Delta} = 4$ mesh and a $R_f/\overline{\Delta} = 8$ mesh. The same detachment dynamics was obtained, leading us to think that mesh discrepancy can be discarded. Another possible reason could be the difference between the imposed and measured contact angle in our simulations. As illustrated on Fig. 23, the average measured angle is always below the imposed angle $\theta_{eq} = 10°$, with an error sometimes above 50%. This angle is not given in [57], but one can guess that the detachment dynamics depends on the contact angle imposition accuracy. The improvement of the contact angle imposition for near-total wetting situations could be an improvement, but is beyond the scope of this paper.

We now turn to the numerical determination of the critical radius for different fiber radii. In order to ease visualization of the results, the Eötvös number is defined as

$$Eo = \frac{\frac{4}{3}\pi R_d^3 \Delta\rho g}{4\sigma\pi R_f}, \tag{55}$$

where R_d is the initial drop radius [57]. This dimensionless number compares the weight of liquid to the maximum surface tension force among all possible configurations of the drop on the fiber [36]. It should be noted that the weight considered in Eq. (55) corresponds to the weight of the initial drop if it was not

crossed by the fiber (overestimation of the drop mass). Results are summed-up in Fig. 25 as a function of the Eötvös number and the normalized fiber radius. A simulation is represented by a circle if the

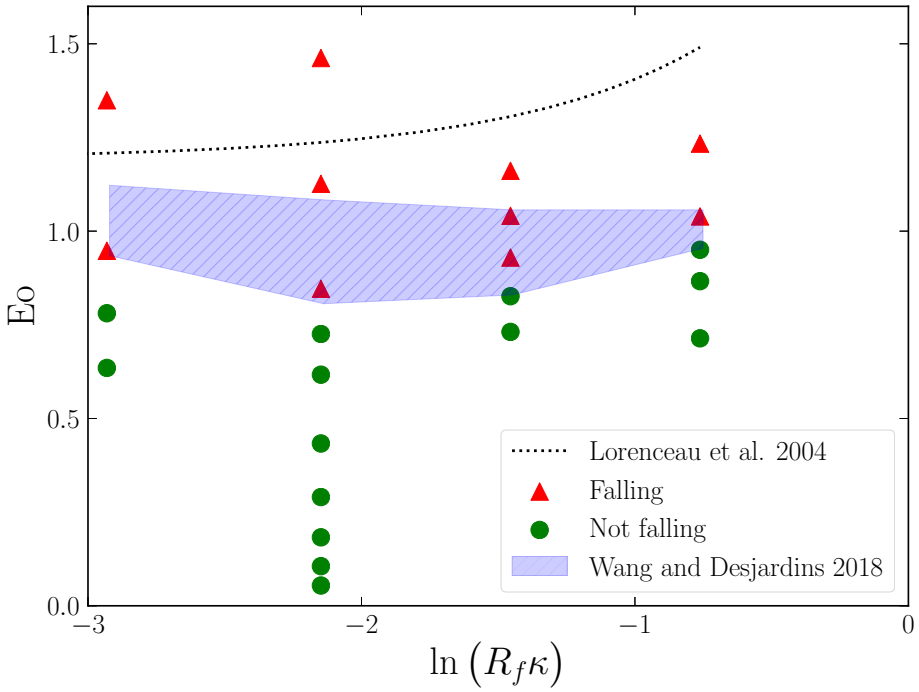

Figure 25: Regime map for gravity-driven detachment from a fiber. The critical Eötvös number determined by Lorenceau et al. [36] (best fit of experimental data) and the transition region determined by Wang and Desjardins [57] are shown for comparison.

drop remains attached to the fiber and by a triangle if the drop falls. In addition, the region between falling drops and not falling drops determined by the simulations of [57] is represented by the shaded area. The experimental results of [36] are also represented. However in [36] the critical radius is determined as $R_c = \left(\frac{3V_c}{4\pi}\right)^{1/3}$, where V_c is the measured critical liquid volume. Therefore, R_c does not correspond to R_d in Eq. (55). We determine the drop initial radius R_d of a drop centered on the fiber corresponding to a liquid volume V_c. If we approximate the volume of the fiber inside the drop by a cylinder, we have

$$V_c = \frac{4}{3}\pi R_d^3 - 2\pi R_f^2 R_d. \tag{56}$$

Using the second case of Eq. (54) and $V_c = \frac{4}{3}\pi R_c^3$ we obtain

$$R_d\left(\frac{2R_d^2}{3} - R_f^2\right) = \frac{2}{3}1.53^3 R_f \kappa^{-2}, \tag{57}$$

which is solved numerically for R_d. The Eötvös number is finally computed to plot the curve in Fig. 25. One major consequence of this modification is that the critical Eötvös number varies with the fiber radius, which would not be the case if the approximation $R_d = R_c$ had been done.

Even if the critical Eötvös number appears to be slightly different between the three studies, the uncertainty on the experimental data covers this gap, as shown hereafter. Indeed, the critical radius determined experimentally by [36] through a best fit of the results is actually $R_c = 1.53 R_f^{1/3\pm0.1}\kappa^{-2/3\pm0.1}$. For $R_f = 350$ µm (third column on Fig. 25), we find $0.87 < Eo_{expe} < 1.98$, making the results of [57] and ours consistent with the experiments. Furthermore, as noted by [36], the experimentally determined critical radius may be overestimated since liquid is added until the drop detaches. Their critical radius corresponds thus to the smallest falling drop for each fiber. On the other hand, the disequilibrium induced by the initial position of the spherical drop centered on the fiber in our simulations can lead to an underestimated critical radius. We verified the influence of the initial drop position by shifting the drop center under the fiber at a distance $R_d/2$ from the fiber axis, case in which the initial disequilibrium is less important. Note that the liquid volume is slightly higher than for the centered drop since the fiber does not cross the initial drop through its center. In this case the drop with $R_d = 1300$ µm remains

attached to the fiber with $R_f = 350$ µm whereas it detaches when initialized centered, showing the strong influence of the initial condition on this test case.

4.6.2. Surface tension-driven detachment from a horizontal fiber

A last numerical experiment is presented here. The detachment of liquid from a hydrophobic fiber can be initiated by surface energy release during the coalescence of two drops. As explained by Liu et al. [33, 34, 35], while the coalescence of two quiescent drops does not move the mass center of the liquid, breaking the symmetry of the oscillations caused by drop coalescence can be used to convert surface energy into kinetic energy. For this purpose, a solid surface may be smartly employed to force the resulting drop movement into one direction. For instance, Zhang et al. [62] performed experiments and 2D simulations of self-propelled removal of drops from a hydrophobic fiber. This case has been recently simulated in 3D by Wang and Desjardins [57] on a cartesian grid with an immersed boundary method.

The experimental setup is the following: two barely touching drops are located on both sides of a fiber. The fiber does not lie between the two drop centers of mass, but it is slightly decentered to create an asymmetry, as illustrated on the first column of Fig. 26. The drop centers are situated at a distance $2R_f$ above the fiber axis. The physical parameters are given in Table 10. It corresponds to water drops

Drop radius	R_d	249 µm
Fiber radius	R_f	46 µm
Gas density	ρ_g	1 kg.m^{-3}
Liquid density	ρ_l	1000 kg.m^{-3}
Gas viscosity	μ_g	1×10^{-5} kg.s^{-1}.m^{-1}
Liquid viscosity	μ_l	1×10^{-3} kg.s^{-1}.m^{-1}
Surface tension	σ	0.072 N.m^{-1}
Contact angle	θ_{eq}	120°

Table 10: Parameters for surface tension-driven detachment from a horizontal hydrophobic fiber.

surrounded by air and attached to a teflon-coated copper fiber. The capillary length κ^{-1} has the standard value of 2.7 mm for air-water interface. Drops radius being about ten times smaller than κ^{-1}, gravity has a negligible effect. As an illustration, gravity has been considered in the simulation, horizontally oriented on Fig. 26, but no effect is noticeable. As in [57], the mesh in the area of interest is such that there are 5 cells accross the fiber diameter. But, contrary to [57] where 16 000 000 uniform cells are required, in our case the number of cells stays below 1 800 000 during the whole simulation thanks to dynamic mesh adaptation.

The dynamics of the coalescence and the self-removal of the drop is represented on Fig. 26. Our

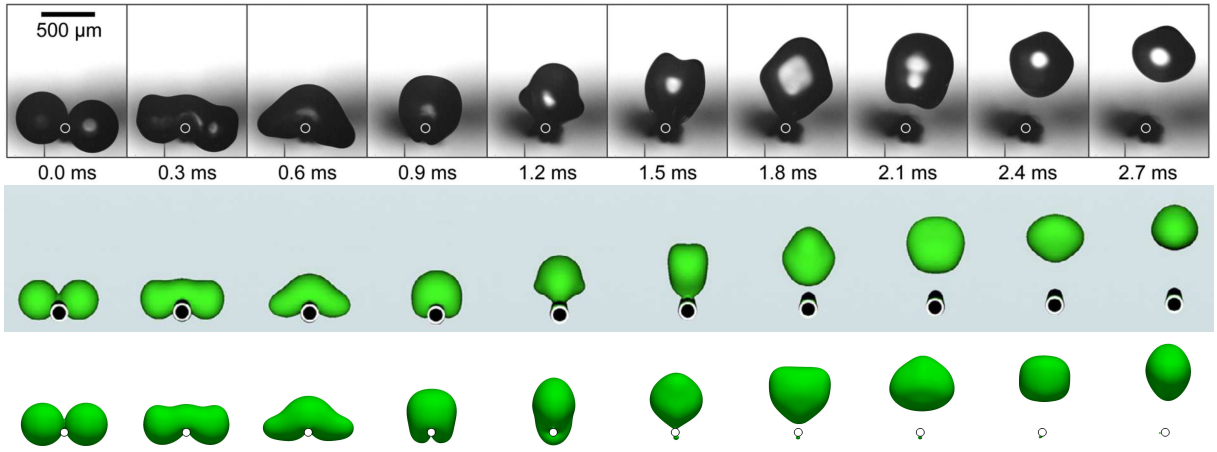

Figure 26: Coalescence of two droplets on a hydrophobic fiber. The upper images are from the experiments of [62], the middle images are from the simulations of [57] and the lower images are from our simulations.

simulation is compared to the experiments of [62] and the simulations of [57]. The time interval between each snapshot is the same for the three studies. Our simulation reveals a rather good agreement with the previous studies, especially at the beginning of the coalescence. Nonetheless, a significant discrepancy between our studies and previous ones can be observed on the fifth snapshot of Fig. 26. In our simulation, a liquid bridge is formed under the fiber when the two liquid growths merge. As a consequence, the

oscillations are broken and the shape of the resulting drop is different. A small amount of liquid stays under the fiber after the detachment. This difference may be explained by discrepancies in the exact initial position of the drops, which is not specified in previous studies. The overall dynamics is however not affected since the detachment occurs at the same physical time. Through visual analysis of the snapshots from [57], reported in Fig. 26, one may also argue that the fiber radius seems larger than the value given therein. We have thus performed a simulation with a fiber radius of $R_f = 60$ µm and report the result in AppendixE. A better qualitative agreement with experiments of [62] and simulations of [57] is found. The simulations show excellent conservation properties with a mass error below 0.15%. A slice perpendicular to the fiber and passing through the drops centers is represented on Fig. 27, showing the mesh and the level-set field. The dynamic mesh adaptation enables to follow the interface with fine cells and coarsen the mesh when the interface moves away.

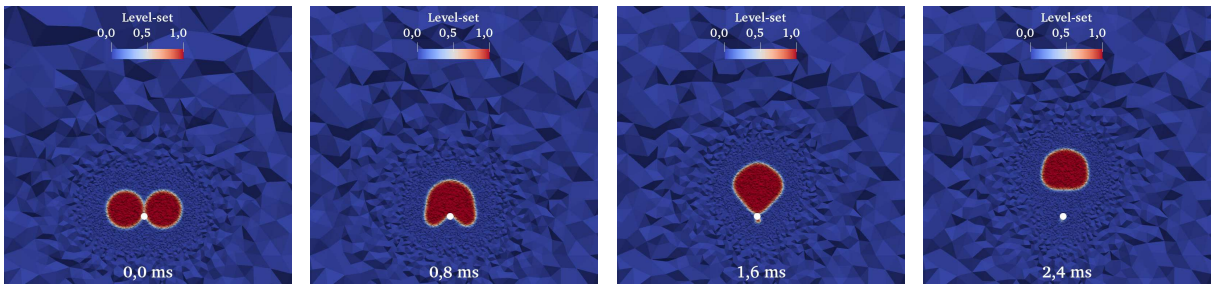

Figure 27: Slices of the coalescence of two droplets on a hydrophobic fiber. The mesh cells and the level-set field are represented.

5. Conclusions

In this study, a numerical methodology has been implemented in the code YALES2 to simulate contact lines on simplicial unstructured grids. The conservative level-set enables an accurate transport of the interface and improves mass conservation properties compared to the standard signed distance level-set. The contact angle is imposed implicitely by modifying the interface curvature at contact line, avoiding artificial movement of the contact line. A simple partial slip condition has been implemented to alleviate the contact line paradox. In order to compute accurately the interface normal vector and the curvature close to the wall, the signed distance function is extended in the obtuse side of the contact angle. High-order differential operators for unstructured meshes are employed for the Taylor series expansions. The method is first used to assess contact angle imposition on a simple but stringent 2D test case. A good accuracy similar to previous results on cartesian grids is obtained for non-extreme contact angles. The robustness of the method is then evaluated with the impact of a drop on a sphere. The qualitative and quantitative behaviour are consistent with the literature and excellent mass conservation is demonstrated. The spreading dynamics is studied afterwards, showing consistency with previous experimental and numerical work. Finally, the drop detachment from a fiber is simulated. A good agreement with literature is found, within the error margin created by the unknown initialization in previous studies. Dynamic mesh adaptation enables to strongly reduce the number of mesh cells (typically one order of magnitude) compared to a homogenous cartesian grid in addition to the capability of the unstructured mesh to fit any complex boundary without using an immersed boundary method. The presented methodology is thus robust and can be used for predictive simulations of contact lines on complex geometries.

Acknowledgments

This work has been supported by the french Ministry of Higher Education, Research and Innovation. The GENCI (Grant 2A00611) and the third edition of the Extreme CFD Workshop are gratefully acknowledged. The authors would like to thank Vincent Moureau, Ghislain Lartigue and Pierre Bénard for providing the code YALES2, Romain Janodet and Mélody Cailler for helpful discussions on level-set re-initialization and dynamic mesh adaptation and Guillaume Sahut for his precious advices concerning two-phase flows simulations.

AppendixA. Laminar single-phase flow with Navier slip boundary condition

The theoretical solution for a 2D Poiseuille flow with Navier slip boundary conditions on the walls can be easily derived from Navier-Stokes equations. Without loss of generality, we make the assumption

that x is the streamwise coordinate and y is the flow normal coordinate. The origin is located at the center of the inlet. The theoretical streamwise velocity is given by

$$u^{th}(y) = \frac{-U_I}{H\left(H/3+\lambda\right)}\left(\frac{y^2}{2} - \frac{H^2}{2} - \lambda H\right), \tag{A.1}$$

with H the channel half height, U_I the inlet uniform velocity and λ the slip length. Due to the slip condition, the wall velocity is non-zero and reads

$$u_{wall} = \frac{\lambda}{H/3+\lambda} U_I. \tag{A.2}$$

The physical parameters are set as follows: $U_I = 0.01$ m/s, $H = 0.01$ m, $\lambda = 0.002$ m, $\rho = 1$ kg/m^3 and $\mu = 10^{-5}$ kg/m/s. The Reynolds number is $Re = 20$. The simulations are performed on unstructured grids composed of triangular elements. At stationnary state, the streamwise velocity profile is extracted at the channel mid-length. The profile is plotted on Fig. A.28a for different cell sizes $\overline{\Delta}$. A good agreement with the theoretical solution is found. The relative errors are plotted against mesh resolution on Fig. A.28b. The errors are defined as

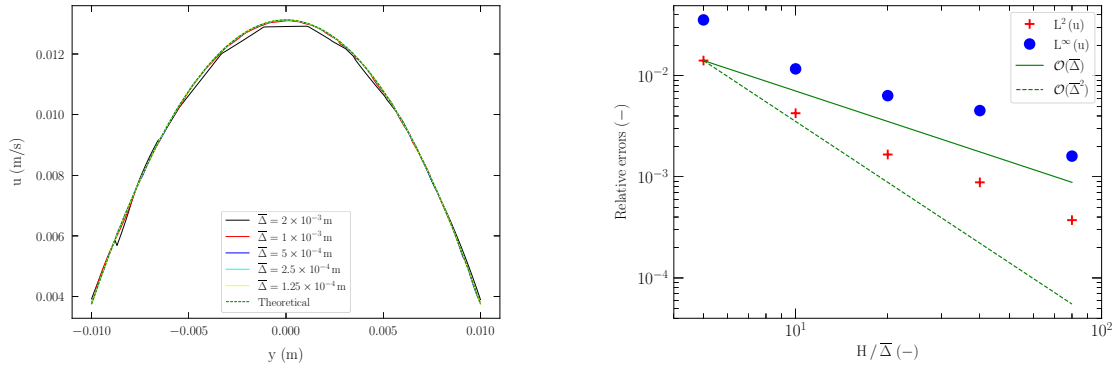

(a) (b)

Figure A.28: (a) Streamwise velocity profile for a 2D Poiseuille flow with Navier slip boundary condition. (b) Error and convergence order of the velocity profile.

$$L^\infty(u) = \max_{i \in N_p} |u^{th}(y_i) - u(y_i)|, \tag{A.3}$$

$$L^2(u) = \sqrt{\frac{1}{N_p}\sum_{i=1}^{N_p}\left(u^{th}(y_i) - u(y_i)\right)^2}, \tag{A.4}$$

where N_p is the number of points of the extracted profile. This quantities are normalized by U_I. For both norms, a first order convergence is observed. This is consistent with the first order discretization of the wall velocity gradient given in Eq. (16).

AppendixB. Curvature evaluation at contact line in 3D

The 2D test performed in section 3.3.3 is extended here to 3D. A spherical interface is initialized, forming an angle θ_{eq} with a flat surface, measured inside the sphere. As in section 3.3.3, the curvature at contact line is computed from the geometrical distance or the analytical distance outside the Blind Spot, both with extensions in the Blind Spot. The angles $\theta_{eq} = 20°$ with radius $R_0 = 0.045$ m and $\theta_{eq} = 160°$ with radius $R_0 = 0.01$ m are simulated on five meshes identified by the average cell size $\overline{\Delta}$. The relative errors are defined as

$$L^\infty(\mathcal{K}_{CL}) = \frac{1}{\mathcal{K}^{th}_{CL}} \max_{ik \in N_{CL}} |\mathcal{K}^{th}_{CL} - \mathcal{K}^{ik}_{CL}|, \tag{B.1}$$

$$L^2(\mathcal{K}_{CL}) = \frac{1}{\mathcal{K}^{th}_{CL}} \sqrt{\frac{1}{N_{CL}}\sum_{ik=1}^{N_{CL}}\left(\mathcal{K}^{th}_{CL} - \mathcal{K}^{ik}_{CL}\right)^2}, \tag{B.2}$$

$\overline{\Delta}$ (m)	4×10^{-3}	2×10^{-3}	1×10^{-3}	5×10^{-4}	2.5×10^{-4}
$L^{\infty}(\mathcal{K}_{CL})$	8.80%	5.94%	9.68%	41.70%	13.86%
$L^{2}(\mathcal{K}_{CL})$	6.28%	2.81%	2.77%	4.86%	3.45%

Table B.11: Curvature relative error at contact line for a contact angle $\theta_{eq} = 20°$ in 3D. The distance outside the Blind Spot is computed with the geometrical algorithm.

$\overline{\Delta}$ (m)	4×10^{-3}	2×10^{-3}	1×10^{-3}	5×10^{-4}	2.5×10^{-4}
$L^{\infty}(\mathcal{K}_{CL})$	8.19%	3.43%	1.56%	0.81%	0.40%
$L^{2}(\mathcal{K}_{CL})$	6.01%	2.31%	1.03%	0.47%	0.23%

Table B.12: Curvature relative error at contact line for a contact angle $\theta_{eq} = 20°$ in 3D. The distance outside the Blind Spot is the analytical distance to the spherical interface.

$\overline{\Delta}$ (m)	4×10^{-3}	2×10^{-3}	1×10^{-3}	5×10^{-4}	2.5×10^{-4}
$L^{\infty}(\mathcal{K}_{CL})$	32.72%	8.01%	7.56%	7.84%	9.88%
$L^{2}(\mathcal{K}_{CL})$	28.04%	5.11%	2.77%	3.59%	3.56%

Table B.13: Curvature relative error at contact line for a contact angle $\theta_{eq} = 160°$ in 3D. The distance outside the Blind Spot is computed with the geometrical algorithm.

$\overline{\Delta}$ (m)	4×10^{-3}	2×10^{-3}	1×10^{-3}	5×10^{-4}	2.5×10^{-4}	1.25×10^{-4}
$L^{\infty}(\mathcal{K}_{CL})$	34.88%	11.85%	3.26%	1.52%	1.18%	0.78%
$L^{2}(\mathcal{K}_{CL})$	30.88%	7.46%	1.30%	0.71%	0.70%	0.41%

Table B.14: Curvature relative error at contact line for a contact angle $\theta_{eq} = 160°$ in 3D. The distance outside the Blind Spot is the analytical distance to the spherical interface.

with $\mathcal{K}_{CL}^{th}$ the theoretical curvature evaluated at contact line, $\mathcal{K}_{CL}^{ik}$ the computed curvature at edge ik and N_{CL} the number of edges crossed by the contact line. The errors are gathered in Table B.11, B.12, B.13 and B.14.

No clear convergence with mesh refinement is observed for both norms when the geometrical distance is considered. As in 2D, this is due to the second-order geometrical distance. Nevertheless, the L^2 error remains below 5% except for the coarsest meshes. When the extensions are based on the analytical distance, both norms exhibit convergence with mesh refinement. An additional simulation on a finer mesh has been performed for $\theta_{eq} = 160°$ with analytical distance. For this case, the convergence order is below one for fine meshes. However, to the best of the authors' knowledge, quantification of the curvature error at contact line on 3D unstructured meshes does not exist in the literature. These results constitute therefore a milestone towards the accurate treatment of capillary terms at contact line on unstructured grids.

AppendixC. Time convergence study on 2D capillary rise

A time convergence study is performed for the capillary rise with $\Omega = 1$ and $\lambda = R/5$ on the coarsest mesh defined by $\overline{\Delta} = R/10$. The apex height is plotted against time on Fig. C.29, for five arbitrary time steps and for the time step given by the stability constraint Eq. (33). The results obtained by Gründing

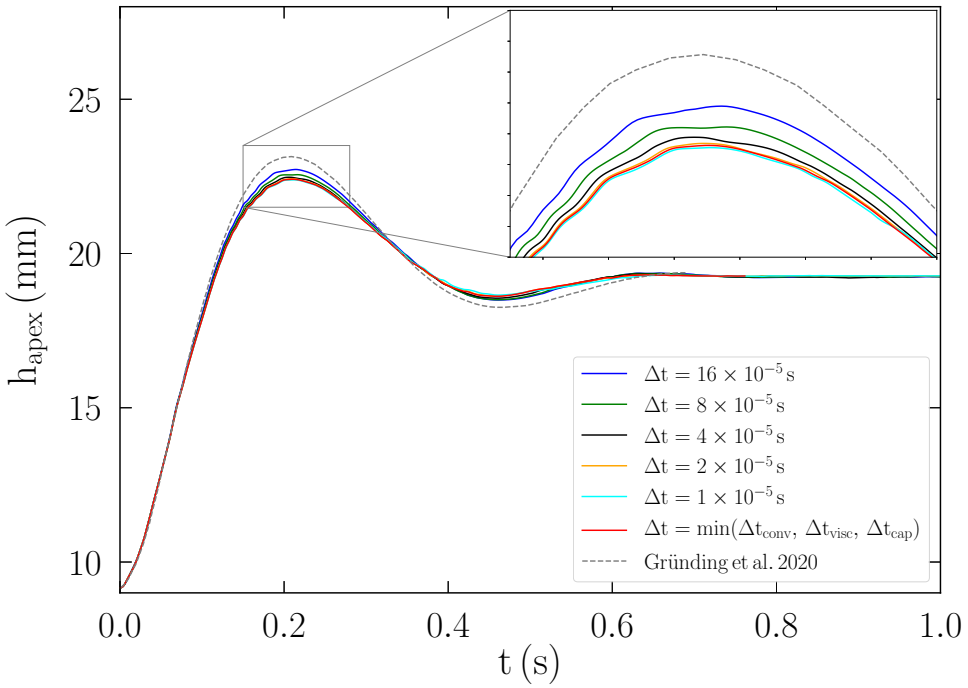

Figure C.29: Time evolution of the height of the meniscus apex for various time steps with cell size $\overline{\Delta} = R/10$.

et al. [21] with a geometric Volume of Fluid solver on a mesh such that $\overline{\Delta} = R/128$ are also represented. It can be seen that the results obtained for the simulation using the automated procedure of time step determination (as minimum of the three stability criteria) coincide almost with the smallest imposed time steps. This means that the solution obtained with the computed time step is already converged in time. Further decreasing the time step would have no impact on the solution. One can notice that our results do not converge toward the results of [21]. This can be explained by the important spatial error due to the coarser mesh. The mesh convergence study presented in section 4.3 confirms that our results converge toward those of [21] when refining the mesh.

AppendixD. Dynamics of a 3D drop impact on a flat wall

We reproduce here the experiment of Šikalo et al. [50] where the impact of a glycerin drop on a glass wall is studied. The physical parameters are gathered in Table D.15. The equilibrium angle θ_{eq} is an approximation of the advancing contact angle $\theta_a = 17°$ and the receding contact angle $\theta_r = 13°$ given

Drop radius	R_0	0.001225 m
Gas density	ρ_g	1 kg.m^{-3}
Liquid density	ρ_l	1220 kg.m^{-3}
Gas viscosity	μ_g	10^{-5} kg.s^{-1}.m^{-1}
Liquid viscosity	μ_l	0.116 kg.s^{-1}.m^{-1}
Surface tension	σ	0.063 N.m^{-1}
Contact angle	θ_{eq}	15°
Impact velocity	V_0	1.41 m.s^{-1}

Table D.15: Parameters for the impact of a 3D glycerin drop on a flat glass wall.

in [50]. Initially, the drop has an impact velocity V_0 perpendicular to the wall and touches the wall in one point. Gravity is oriented towards the wall and has the value $g = 9.81$ m.s^{-2}. In our simulations the mesh size is defined by $\overline{\Delta} = 48.4$ µm $\simeq R_0/25$. The simulations have been performed once with a resolved slip length $\lambda = \overline{\Delta}$ and once with an underresolved slip length $\lambda = 10^{-9}$ m. The normalized contact line diameter is plotted against normalized time in log-log scale on Fig. D.30. The experimental results of [50]

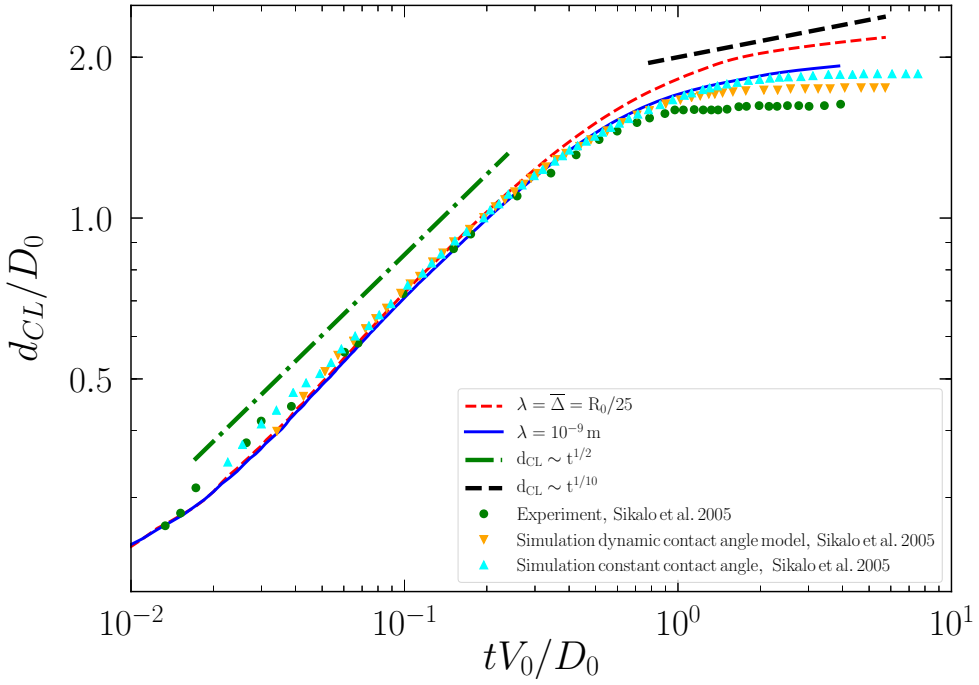

Figure D.30: Normalized contact line diameter versus normalized time for the impact of a 3D glycerin drop on a flat glass wall.

as well as 2D axisymmetric simulations of the same authors are represented. The characteristic mesh size is $\overline{\Delta} = 19.5$ µm. In [50], the simulations were performed using either a dynamic contact angle model or a constant contact angle. We can notice that all the results collapse on one curve during the inertial spreading. As observed by [58] the contact line diameter scales as the square root of time. During the last phase of spreading, however, significant differences appear. First, it must be noted that the viscous spreading does not follow Tanner's law for the experiment, which is considered as a reference here. It may be explained by the fact that the surface wettability is not high enough for Tanner's law to be applicable [54] and by the gravity effects which are non-negligible. As a matter of fact, the drop radius is of the order of the capillary length $\kappa^{-1} = \sqrt{\sigma/(\rho_l g)} = 2.29$ mm.

Furthermore, using an overestimated slip length $\lambda = \overline{\Delta}$ in our simulation leads to an overestimation of the contact line diameter at a given instant of the viscous spreading. Indeed, the higher the slip length, the higher the contact line velocity, i.e. the faster the spreading. A realistic but underresolved slip length $\lambda = 10^{-9}$ m lowers this overestimation. However, using an underresolved slip length cannot be satisfactory since it indroduces mesh dependency of the results. Regarding the simulations of [50], using

a dynamic contact angle model enables a closer match with the experiments than a constant contact angle. From these observations, it is clear that in some configurations and on affordable mesh size, a resolved slip length and a constant contact angle are not sufficient to estimate accurately global quantities which depend on underresolved phenomena in the contact line region. The first stage of the spreading is nonetheless accurately simulated without additional modelling.

AppendixE. Coalescence of two drops on a hydrophobic fiber: effect of the fiber radius

Motivated by the visual analysis of the results of [57] reported on Fig. 26 that suggests a fiber radius larger than the value given therein, the case of surface tension-driven detachment from a horizontal fiber presented in section 4.6.2 is reproduced here with a larger fiber radius. The parameters are the same as in section 4.6.2 (see Table 10), except for the fiber radius which is $R_f = 60$ µm. The drop centers are situated at a distance $2.5R_f$ above the fiber axis. The experimental results of [62] and the simulation of [57], both performed with a fiber radius $R_f = 46$ µm, are compared with our simulation with $R_f = 60$ µm on Fig. E.31. A better qualitative agreement with previous studies than for $R_f = 46$ µm is found,

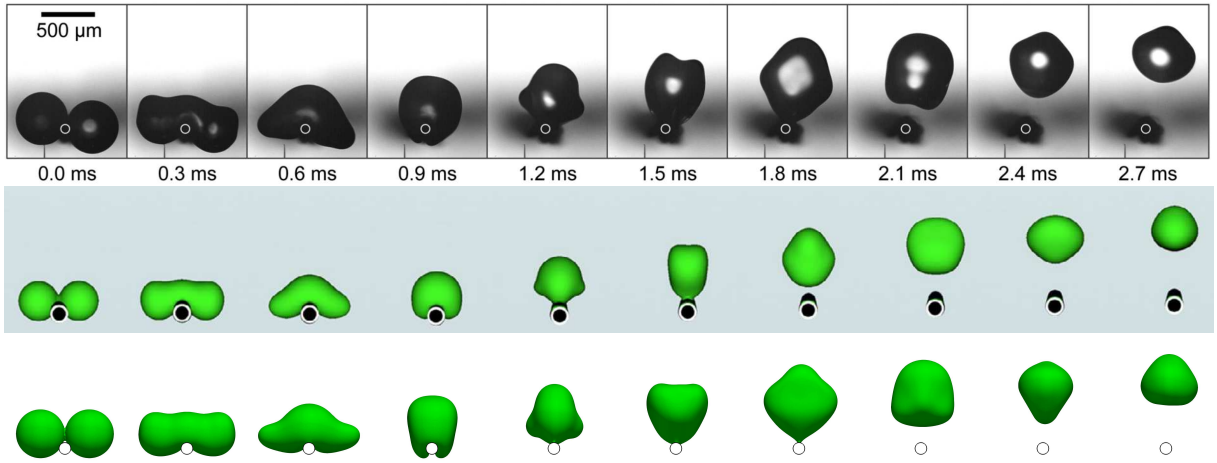

Figure E.31: Droplets coalescence on a hydrophobic fiber. The upper images are from the experiments of [62], the middle images are from the simulations of [57] and the lower images are from our simulations with fiber radius $R_f = 60$ µm.

especially at snapshots 5, 6 and 7. The liquid does not wrap the fiber: the oscillations are therefore not broken. The qualitative behaviour of the detachment is thus highly dependent on the fiber radius.

References

[1] S. Afkhami, S. Zaleski, and M. Bussmann. A mesh-dependent model for applying dynamic contact angles to VOF simulations. *Journal of Computational Physics*, 228:5370–5389, 2009.

[2] M. Bernard, G. Lartigue, G. Balarac, V. Moureau, and G. Puigt. A framework to perform high-order deconvolution for finite-volume methode on simplicial meshes. *International Journal for Numerical Methods in Fluids*, pages 1–33, 2020.

[3] A.L. Biance, C. Clanet, and D. Quéré. First steps in the spreading of a liquid droplet. *Physical Review E*, 69:016301, 2004.

[4] J.U. Brackbill, D.B. Kothe, and C. Zemach. A continuum method for modeling surface tension. *Journal of Computational Physics*, 100:335–354, 1992.

[5] G.C. Buscaglia and R.F. Ausas. Variational formulations for surface tension, capillarity and wetting. *Computer Methods in Applied Mechanics and Engineering*, 200:3011–3025, 2011.

[6] Z. Cao, D. Sun, J. Wei, and B. Yu. A coupled volume-of-fluid and level set method based on multi-dimensional advection for unstructured triangular meshes. *Chemical Engineering Science*, 176:560–579, 2018.

[7] R. Chiodi and O. Desjardins. A reformulation of the conservative level set reinitialization equation for accurate and robust simulation of complex multiphase flows. *Journal of Computational Physics*, 343:186–200, 2017.

[8] A.J. Chorin. A numerical method for solving incompressible viscous flow problems. *Journal of Computational Physics*, 2:12–26, 1967.

[9] A.J. Chorin. Numerical solution of the Navier-Stokes equations. *Mathematics of Computation*, 22:745–762, 1968.

[10] P.G. de Gennes. The dynamics of a spreading droplet. *Comptes-rendus des séances de l'Académie des sciences. Série 2, Mécanique-physique, chimie, sciences de l'univers, sciences de la terre*, 298:111–115, 1984.

[11] P.G. de Gennes, F. Brochard-Wyart, and D. Quéré. *Capillarity and Wetting Phenomena. Drops, Bubbles, Pearls, Waves*. Springer, 2002.

[12] D. Deganello, A.J. Williams, T.N. Croft, A.S. Lubansky, D.T. Gethin, and T.C. Claypole. Level-set method for the modelling of liquid bridge formation and break-up. *Computers & Fluids*, 40:42–51, 2011.

[13] G. Della Rocca and G. Blanquart. A level set based method to simulate contact line motion and dynamic contact angles for multiphase flow. In *Seventh International Conference on Computational Fluid Dynamics (ICCFD7), Big Island, Hawaii*, page 2106, July 2012.

[14] G. Della Rocca and G. Blanquart. Level set reinitialization at contact line. *Journal of Computational Physics*, 265:34–49, 2014.

[15] O. Desjardins, V. Moureau, and H. Pitsch. An accurate conservative level set/ghost fluid method for simulating turbulent atomization. *Journal of Computational Physics*, 227:8395–8416, 2008.

[16] M. Dianat, M. Skarysz, and A. Garmory. A Coupled Level set and Volume of Fluid method for automotive exterior water management applications. *International Journal of Multiphase Flow*, 91:19–38, 2017.

[17] J.B. Dupont and D. Legendre. Numerical simulation of static and sliding drop with contact angle hysteresis. *Journal of Computational Physics*, 229:2453–2478, 2010.

[18] R. P. Fedkiw, T. Aslam, B. Merriman, and S. Osher. A non-oscillatory eulerian approach to interfaces in multimaterial flows (the ghost fluid method). *Journal of Computational Physics*, 152(2):457–492, 1999.

[19] P. Gao and J.J. Feng. A numerical investigation of the propulsion of water walkers. *Journal of Fluid Mechanics*, 668:363–383, 2010.

[20] R. Goldman. Curvature formulas for implicit curves and surfaces. *Computer Aided Geometric Design*, 22:632–658, 2005.

[21] D. Gründing, M. Smuda, T. Antritter, M. Fricke, D. Rettenmaier, F. Kummer, P. Stephan, H. Marschall, and D. Bothe. A comparative study of transient capillary rise using direct numerical simulations. *Applied Mathematical Modelling*, 86:142–165, 2020.

[22] H. Huang, D. Liang, and B. Wetton. Computation of a moving drop/bubble on a solid surface using a front-tracking method. *Communications in Mathematical Sciences*, 2:535–552, 2004.

[23] C. Huh and L.E. Scriven. Hydrodynamic model of steady movement of a solid/liquid/fluid contact line. *Journal of Colloid and Interface Science*, 35:85–101, 1971.

[24] D. Jacqmin. Contact-line dynamics of a diffuse fluid interface. *Journal of Fluid Mechanics*, 402:57–88, 2000.

[25] R. Janodet, G. Vaudor, G. Lartigue, P. Benard, V. Moureau, and R. Mercier. An unstructured conservative level-set algorithm coupled with dynamic mesh adaptation for the computation of liquid-gas flows. In *29th European Conference on Liquid Atomization and Spray Systems (ILASS Europe), Paris, France*, September 2019.

[26] J. Jurin. An account of some experiments shown before the royal society; with an enquiry into the cause of the ascent and suspension of water in capillary tubes. *Philosophical Transactions of the Royal Society of London*, 30(355):739–747, 1718.

[27] J. Koplik, J.R. Banavar, and J.F. Willemsen. Molecular dynamics of Poiseuille flow and moving contact lines. *Physical Review Letters*, 60:1282–1285, 1988.

[28] M. Kraushaar. *Application of the compressible and Low-Mach number approaches to large-eddy simulation of turbulent flows in aero-engines*. PhD thesis, Institut National Polytechnique de Toulouse, 2011.

[29] E. Lauga, M. Brenner, and H. Stone. *Springer Handbook of experimental fluid mechanics*, chapter Microfluidics: the no-slip boundary condition, pages 1219–1240. Springer, Berlin, Heidelberg, 2007.

[30] D. Legendre and M. Maglio. Comparison between numerical models for the simulation of moving contact lines. *Computers & Fluids*, 113:2–13, 2015.

[31] J. Leparoux, R. Mercier, V. Moureau, and H. Musaefendic. Primary atomization simulation applied to a jet in crossflow aeronautical injector with dynamic mesh adaptation. In *14th Triennal International Conference on Liquid Atomization and Spray Systems (ICLASS), Chicago, IL, USA*, July 2018.

[32] N. Linder, A. Criscione, I.V. Roisman, H. Marschall, and C. Tropea. 3D computation of an incipient motion of a sessile drop on a rigid surface with contact angle hysteresis. *Theoretical and Computational Fluid Dynamics*, 29:373–390, 2015.

[33] F. Liu. *Surface Energy Powered Processes upon Drop Coalescence*. PhD thesis, Duke University, 2015.

[34] F. Liu, G. Ghigliotti, J.J. Feng, and C.-H. Chen. Numerical simulations of self-propelled jumping upon drop coalescence on non-wetting surfaces. *Journal of fluid mechanics*, 752:39, 2014.

[35] F. Liu, G. Ghigliotti, J.J. Feng, and C.-H. Chen. Self-propelled jumping upon drop coalescence on leidenfrost surfaces. *Journal of fluid mechanics*, 752:22, 2014.

[36] É. Lorenceau, C. Clanet, and D. Quéré. Capturing drops with a thin fiber. *Journal of Colloid and Interface Science*, 279:192–197, 2004.

[37] J. Luo, H.Y. Hu, and N.A. Adams. Curvature boundary condition for a moving contact line. *Journal of Computational Physics*, 310:329–341, 2016.

[38] M. Malandain. *Simulation massivement parallèle des écoulements turbulents à faible nombre de Mach*. PhD thesis, INSA de Rouen, 2013.

[39] M. Malandain, N. Maheu, and V. Moureau. Optimization of the deflated Conjugate Gradient algorithm for the solving of elliptic equations on massively parallel machines. *Journal of Computational Physics*, 238:32–47, 2013.

[40] S. Manservisi and R. Scardovelli. A variational approach to the contact angle dynamics of spreading droplets. *Computers & Fluids*, 38:406–424, 2009.

[41] V. Moureau, P. Domingo, and L. Vervisch. Design of a massively parallel cfd code for complex geometries. *Comptes Rendus Mecanique*, 339(2):141–148, 2011.

[42] E. Olsson and G. Kreiss. A conservative level set method for two phase flow. *Journal of Computational Physics*, 210:225–246, 2005.

[43] E. Olsson, G. Kreiss, and S. Zahedi. A conservative level set method for two phase flow II. *Journal of Computational Physics*, 225:785–807, 2007.

[44] S. Osher and J.A. Sethian. Fronts propagating with curvature-dependent speed: algorithms based on hamilton–jacobi formulations. *Journal of Computational Physics*, 79:12–49, 1988.

[45] C.S. Peskin. Flow patterns around heart valves : A numerical method. *Journal of Computational Physics*, 10:252–271, 1972.

[46] M. Renardy, Y. Renardy, and J. Li. Numerical simulation of moving contact line problems using a Volume-of-Fluid method. *Journal of Computational Physics*, 171:243–263, 2001.

[47] A.A. Saha and S.K. Mitra. Effect of dynamic contact angle in a volume of fluid (VOF) model for a microfluidic capillary flow. *Journal of Colloid and Interface Science*, 339:461–480, 2009.

[48] G. Sahut, G. Ghigliotti, G. Balarac, M. Bernard, V. Moureau, and P. Marty. Numerical simulation of boiling on unstructured grids. *Journal of Computational Physics*, 432:110161, 2021.

[49] Y. Sato and B. Ničeno. A new contact line treatment for a conservative level set method. *Journal of Computational Physics*, 231:3887–3895, 2012.

[50] Š. Šikalo, H.-D. Wilhelm, I.V. Roisman, S. Jakirlić, and C. Tropea. Dynamic contact angle of spreading droplets: Experiments and simulations. *Physics of Fluids*, 17(6):062103, 2005.

[51] Z. Solomenko, P. Spelt, and P. Alix. A level-set method for large-scale simulations of three-dimensional flows with moving contact lines. *Journal of Computational Physics*, 348:151–170, 2017.

[52] P. Spelt. A level-set approach for simulations of flows with multiple moving contact lines with hysteresis. *Journal of Computational Physics*, 207:389–404, 2005.

[53] Y. Sui and P.D.M. Spelt. An efficient computational model for macroscale simulations of moving contact lines. *Journal of Computational Physics*, 242:37–52, 2013.

[54] L.H. Tanner. The spreading of silicone oil drops on horizontal surfaces. *Journal of Physics D: Applied Physics*, 12:1473–1484, 1979.

[55] R. Temam. Une méthode d'approximation de la solution des équations de Navier–Stokes. *Bulletin de la Société Mathématique de France*, 96:115–152, 1968.

[56] G. Tryggvason, R. Scardovelli, and S. Zaleski. *Direct numerical simulation of liquid-gas multiphase flows*. Cambridge University Press, 2011.

[57] S. Wang and O. Desjardins. 3D numerical study of large-scale two-phase flows with contact lines and application to drop detachment from a horizontal fiber. *International Journal of Multiphase Flow*, 101:35–46, 2018.

[58] K.G. Winkels, J.H. Weist, A. Eddi, and J.H. Snoeijer. Initial spreading of low-viscosity drops on partially wetting surfaces. *Physical Review E*, 85:055301, 2012.

[59] B. Xie, P. Jin, H. Nakayama, S. Liao, and F. Xiao. A conservative solver for surface-tension-driven multiphase flows on collocated unstructured grids. *Journal of Computational Physics*, 401:109025, 2020.

[60] T. Young. An Essay on the Cohesion of Fluids. *Philosophical Transactions of the Royal Society of London*, 95:65–87, 1805.

[61] S. Zahedi, K. Gustavsson, and G. Kreiss. A conservative level set method for contact line dynamics. *Journal of Computational Physics*, 228:6361–6375, 2009.

[62] K. Zhang, F. Liu, A.J. Williams, X. Qu, J.J. Feng, and C.H. Chen. Self-propelled droplet removal from hydrophobic fiber-based coalescers. *Physical Review Letters*, 115:074502, 2015.